OAA Technical Memorandum OAR ETL-299

LABORATORY MODELING OF INTERACTIONS BETWEEN WAVES AND FLOWS IN THE UPPER OCEAN

L.A. Ostrovsky (Editor)

Environmental Technology Laboratory
Boulder, Colorado
March 2000

noaa NATIONAL OCEANIC AND ATMOSPHERIC ADMINISTRATION / Oceanic and Atmospheric Research Laboratories

lum outlines the results of the experimental research which has been
99 by the Institute of Applied Physics (IAP) of the Russian Academy of
ramework of the Agreement between IAP and the NOAA Environmental
oratory (ETL).

Head of the Project: V. I. Talanov
Deputy Head: Yu. I. Troitskaya
Program Coordinator: L. A. Ostrovsky
Authors: V. V. Bakhanov, I. S. Dolina, S. A. Ermakov, I. I. Gopalo,
V. I. Kazakov, O. N. Kemarskaya, D. P. Korotkov, I. R. Konnov, S. N. Reznik,
B. V. Serin, I. A. Sergievskaya

NOAA Technical Memorandum OAR ETL-299

LABORATORY MODELING OF INTERACTIONS BETWEEN WAVES AND FLOWS IN THE UPPER OCEAN

L.A. Ostrovsky (Editor)

Environmental Technology Laboratory
Boulder, Colorado
March 2000

UNITED STATES
DEPARTMENT OF COMMERCE
William M. Daley
Secretary

NATIONAL OCEANIC AND
ATMOSPHERIC ADMINISTRATION

D. JAMES BAKER
Under Secretary for Oceans
and Atmosphere/Administrator

Oceanic and Atmospheric
Research Laboratories

David L. Evans
Director

NOTICE

Mention of a commercial company or product does not constitute an endorsement by the NOAA Oceanic and Atmospheric Research Laboratories. Use of information from this publication concerning proprietary products or the test of such products for publicity or advertising purposes is not authorized.

For sale by the National Technical Information Service, 5285 Port Royal Road
Springfield, VA 22061

Contents

Part 1: Turbulent Flow in a Large Stratified Tank

Part 2: Modulation of Nonlinear Surface Waves by an Internal Wave

Abstract

The results of new experimental studies of waves and turbulence in stratified tanks are presented. Two sets of experiments are described below:

1.The behavior of a stratified turbulent shear current created by a flow generator was studied in a large laboratory tank with a thermocline-type temperature stratification. Profiles of the temperature and flow velocities averaged over the turbulent fluctuations were measured. Then the stability of the shear flow was investigated. It was found that above the thermocline, the Richardson number could drop below 1/4, i.e., the flow was potentially dynamically unstable. After the flow velocity exceeded a threshold value, strong oscillations were observed having a narrow spectral peak of about 0.05 Hz and the amplitude proportional to the square root of the flow velocity. The latter features indicate a global instability of the flow with the excitation of an internal wave. A brief discussion of a possible instability mechanism is also presented.

2. Modulation of gravity-capillary surface waves (GCW) by internal waves was studied in a closed (oval) wave tank. A new mechanism of strong "cascade" modulation of small-scale (millimeter to centimeter wavelength range) higher harmonics of a mechanically generated gravity wave is demonstrated. The modulation coefficient of higher-order harmonics significantly exceeds that for the main harmonic. Such a mechanism can explain the strong modulation of scattered radar signals observed in field experiments.

Laboratory Modeling of Interactions Between Waves and Flows in the Upper Ocean

Part 1: Turbulent Flow in a Large Stratified Tank

1. Introduction

Stratified shear flows are a common element of the dynamics of the ocean and atmosphere. Of special importance are intensive currents that can be prone to unstability that, in turn, creates turbulence and strong mixing in a number of geophysical conditions. Such unstable situations were more than once observed in oceanic counterflows, in straits, and in some areas of seasonal thermocline. Another relevant problem is the behavior of turbulent jets and wakes behind moving bodies that can generate internal waves and thus produce surface signatures.

At the same time, field data are rather episodic and uncontrollable, that stimulated laboratory experiments. However, the flows created in known laboratory experiments (see, e.g., Koop and Browand, 1979; Showalter et al., 1994) are of a rather small scale, so that the corresponding Reynolds numbers too small to simulate the oceanic conditions.

The goal of this part of the work was to create and study the turbulent currents in stratified water and their instabilities with generation of waves. The work involved a large thermostratified tank (20 m x 4 m x 2 m) with a controlled thermocline-type stratification which models the upper ocean structure at about 1:100 of spatial scale and about 1:10 of velocity scale. Note that the characteristic Reynolds numbers in our experiments were of the order of 10,000 that is significantly closer to real situations than in previous laboratory experiments, whereas all processes remain fully controllable.

The work in the large thermostratified tank began with the creation of turbulent shear flow in the tank and the study of its main characteristics. It included measurements of the parameters of the turbulent shear flow generated by the flow inductor: temperature and velocity profiles, turbulence levels and spectra, Richardson numbers and study of spatial evolution of the turbulent jet. Then the effect of excitation of self-oscillations of the turbulent shear flow was studied in detail, including:

- study of the space-time structure of disturbances for different regimes of the flow;

- spectral characteristics of the excited oscillations for different regimes of the flow;

- theoretical review of relevant mechanisms of shear flow instabilities, including an explosive instability and the possibilities of its realization under the conditions present in the large tank.

2. Inductor of shear flow

For the purpose of modeling wave-flow interactions, the tank was equipped with a turbulent current generator. The device, called a flow inductor below, was created for production of a stratified shear flow (Fig. 1). Its construction is based on the property of a stable stratified fluid to keep moving at the level corresponding to its density. The overall sizes of the flow inductor are as follows: length 19.75 m, width 4.10 m, height 1.3 m. The device creates water circulation between its shoulders and the working zone as shown in the figure. The range of the flow velocities is 0.01 to 0.5m/s; the range of the rotation frequencies of the engine is 200 to 600 1/s; the consumed power does not exceed 0.5 kW. The main principles of the action and construction of the flow inductor are described in Bogatyrev et al. (1997).

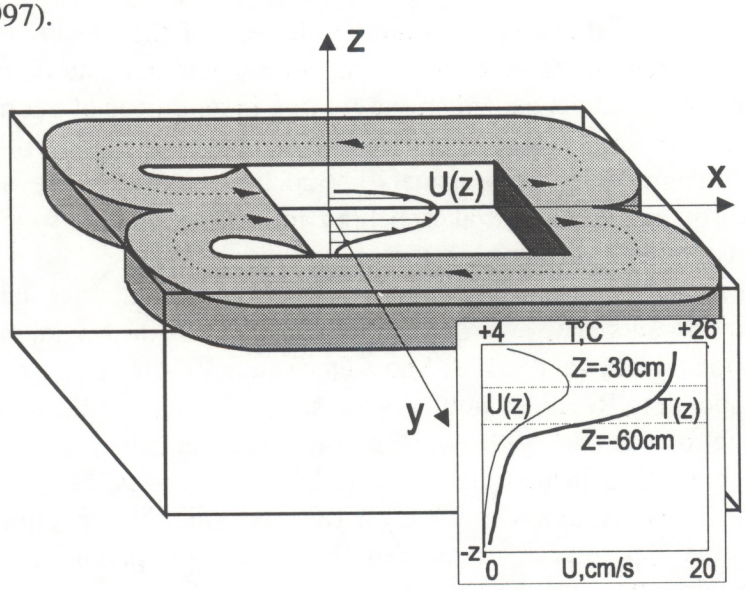

Fig. 1. The scheme of producing shear flow in the experimental tank. Working domain: length - 15.4 m, height - 0.5 m, width - 2.0 m. Mean velocity: up to 20 cm/s. Turbulence level: 5....50%

3. The measuring complex

The information-measuring complex (Fig. 2.) is intended for registration of hydrodynamic processes in a stratified flow and at the water surface of the tank. It includes the primary transformers (sensors); secondary transformers (bridges, amplifiers) and systems of collection, storage, and processing of the information obtained. The necessary software is available for the data collection systems. The complex includes the devices responsible for measurement of variability of temperature and velocity fields in thermostratified fluid and the systems of observation and registration of processes at the water surface.

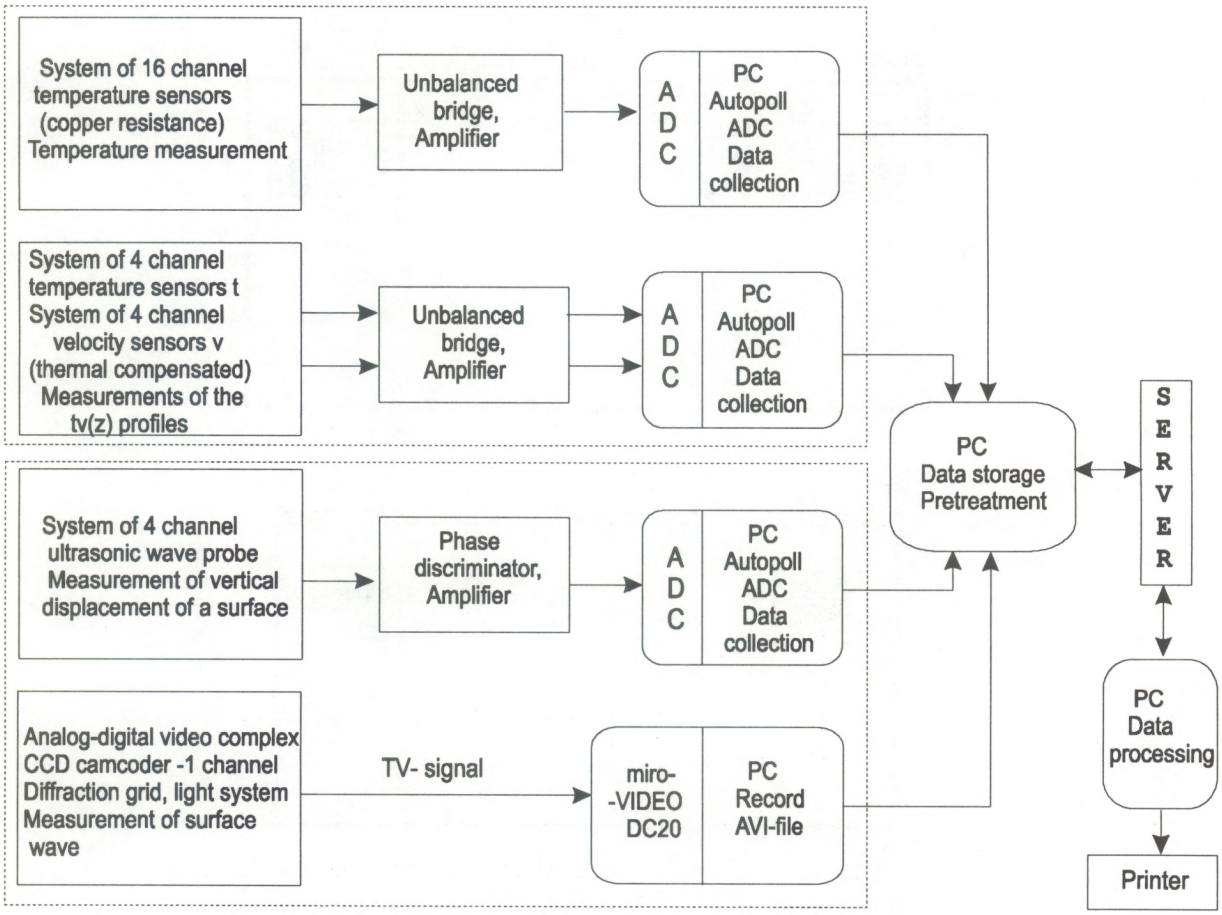

Fig. 2. Block diagram of the information-measuring complex

3.1. Experimental setup (Fig. 3)

Measurements of the variability of the temperature field were carried out by 16-point temperature sensors (electric thermometers). The electric thermometers have a measured temperature range of 0°-30°C with an accuracy of 0.05°C (taking into account the digital noise of the analog-digital converter, ADC); the relaxation time is 0.5 s. Positioning of the electric thermometers depends on a specific experimental task. Typically, as in Fig. 3, they are positioned in the knife-shaped holders placed at the towing trolley. The coordinates of the sensors can be varied within the following limits: x - 0-13 m; y - 0-1 m; z -0-0.9 m.

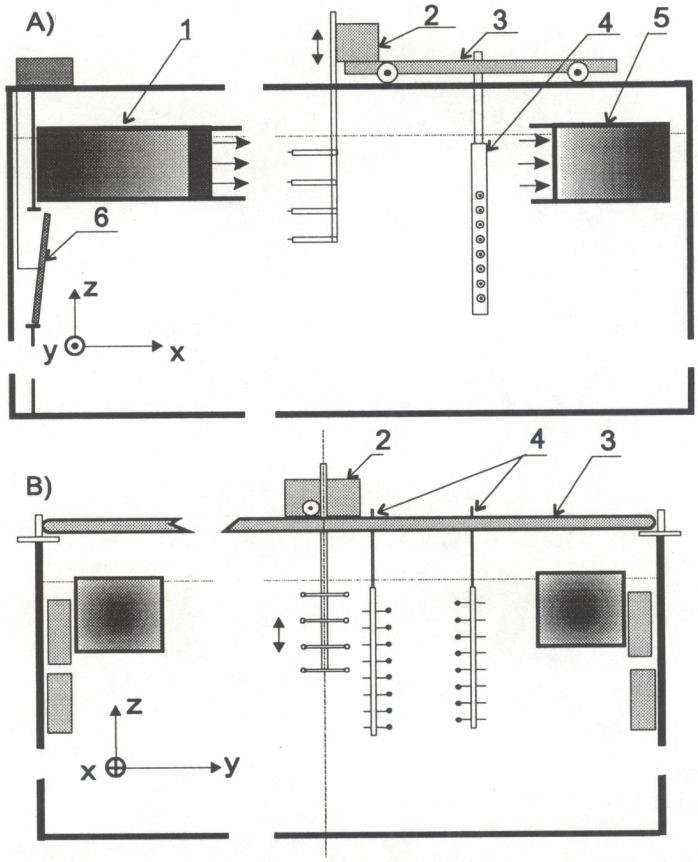

Fig. 3. The study of evolution of shear flow in stratified fluids
1 - output unit of shear flow inductor, 2 - scanning system
with the velocity and temperature probes, 3 - towing trolley,
4 - temperature probes, 5 - input unit of shear flow inductor,
6 - the internal wave maker. A) - side view, B) - front view

Measurement of the mean flow velocity and its turbulent fluctuations was carried out by four hot-wire anemometers. The typical working range of the velocity measurements is 2-20 cm/s for a turbulence level of 5-50% and a frequency of velocity fluctuations less than 1Hz. The anemometers measure the absolute value of the flow velocity. Since the fluid moves mostly in a horizontal direction, the main contribution to the mean velocity is made by the horizontal component (X-axis). The velocity sensors are placed at the bar for measurement of temperature and velocity profiles (see below). The principles of the construction and action of the temperature and velocity sensors are described in our first report (Bogatyrev et al., 1997).

3. 2. The installation for measurement of temperature and velocity profiles

The installation (Fig. 3, position 2) is intended for continuous measurement of distributions of the temperature and velocity over the tank depth. It includes a bar with sensors of temperature and velocity (up to four couples); the sensor of vertical coordinate Z designed on the base of a multi-rotation potentiometer; and the multi-speed reduction

gearbox with an electric engine and the electronic control block. Simultaneous measurement of the temperature and velocity profiles is carried out by the vertical motion of the couple of sensors within a 450 mm vertical interval accompanied by continuous recording of data from the sensors to a PC. For minimum velocity of the sensor motion (approximately 3 mm/s) and sampling frequency 3.3 s^{-1}, the vertical resolution in Z-coordinate is 1mm. The duration of the records of the temperature and velocity profiles is approximately 150s. Besides, the sensors can be stopped at a certain depth for simultaneous recording of temperature and velocity oscillations. The device is fixed at the towing trolley.

4. Creation of the turbulent shear flow in the large tank

4.1. Measurements of parameters of turbulent shear flow generated by the flow inductor: temperature and velocity profiles, turbulence levels and spectra, Richardson numbers.

The temperature and velocity profiles were obtained by vertical scanning of the 85 cm thick domain containing the thermocline with the temperature and velocity sensors (the scanning rate was 0.5 cm/s). Such a regime provided 0.15 cm resolution. Besides, the temperature measurements were carried out with14 hot-wire anemometers placed at the towing trolley (Fig. 3, position 3). The instant temperature and velocity profiles were measured at different x, from 50 cm to 400 cm, with a 50 cm step (x is the horizontal distance from the nozzle) at the central line of the tank. Examples of the instant temperature and velocity profiles are shown in Fig. 4. They obviously have a large variability due to turbulent fluctuations. Thus, to describe their regular characteristics, an averaging is required.

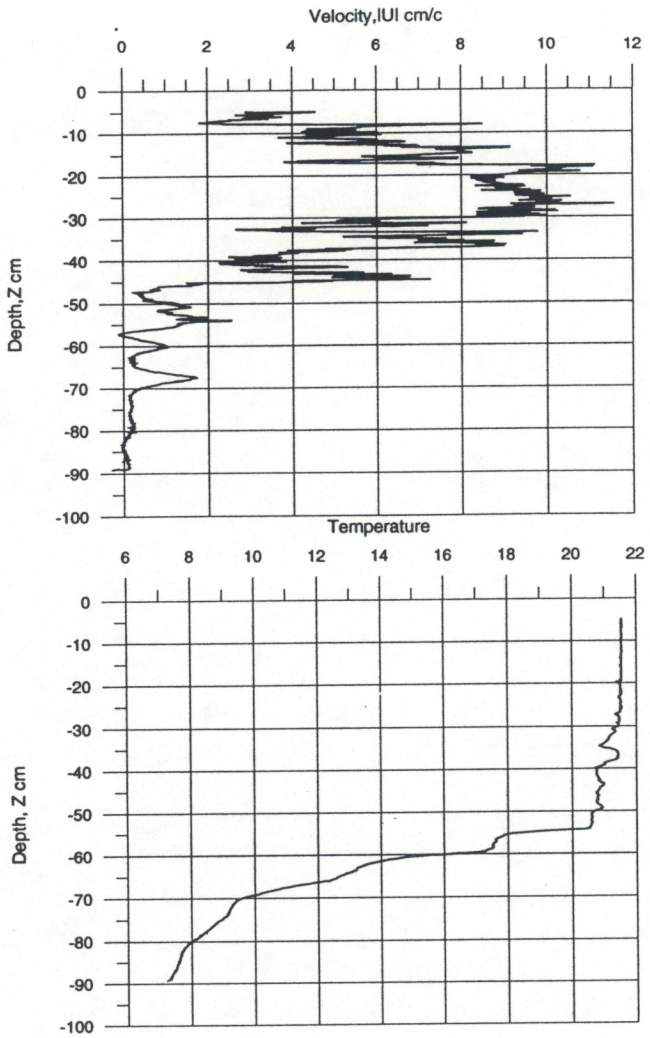

Fig. 4. Examples of instantaneous structures of velocity (above) and temperature (below), measured for x = 200 cm, y = 0

For this purpose, an instant vertical profile of the absolute value of velocity, $|u|(z, t)$, can be presented as the sum of the averaged, $|u|_0$, and oscillating, $|u|_1$, components:

$$|u|^i = |u|_0\left(\frac{z}{L_0}\right) + |u|_1^i\left(\frac{z}{L_1}, \frac{t}{T_1}\right),$$

where L_0 , L_1, and T_1 are the vertical scales of the averaged and fluctuating components of velocity and temperature fluctuations, respectively. Since the scanning sensor is moving with the velocity v, then the measured instant profile (considered as "frozen" during the scanning time) is as follows:

$$|u|^i = |u|_0\left(\frac{z}{L_0}\right) + |u|_1^i\left(\frac{z}{L_1}, \frac{z}{vT_1}\right)$$

In Fig. 4 one can see fluctuations with a length scale less than 10 cm, corresponding to $T_1 v \leq 10$ cm.

The temperature and velocity profiles were measured every 3 min. Since the time correlation scale of the temperature and velocity profiles was less than 25 sec., the random components of the hydrodynamic fields at different profiles were statistically independent. Consequently, the time averaging

$$|u| = \frac{1}{N}\sum_{i=1}^{N}|u|^i,$$

where N is the number of profiles measured, is equivalent to the ensemble averaging, and the dispersion of fluctuations is reduced by $\sqrt{N}$ times. In the present experiment $N = 9$, i.e., the deviation is reduced by approximately 3 times, although it still remains considerable. To further reduce the fluctuations, we used window averaging with the width δ:

$$\overline{|u|} = \frac{1}{2\delta}\int_{z-\delta}^{z+\delta}|u|(z_1)dz. \qquad (1)$$

We choose $2\delta > vT_1$ so that the dispersion, σ_u , of fluctuations with scales less than vT_1 , drops abruptly., i.e.,

$$\sigma_u = \frac{1}{2\delta}\int_{z-\delta}^{z+\delta}|u|_1^i\left(\frac{z_1}{L_1}, \frac{z_1}{vT_1}\right)dz_1 << |u|_1^i.$$

At the same time, the condition $2\delta > vT_1$ leads to the window width 2δ close to the scale of the averaged profile, L_0.

Now we determine the relative error, $|\hat{u}|$, in the averaged profile found in this way. It follows from (1) that $|\hat{u}|$ is an even function of δ, and its Taylor series in δ is

$$|\hat{u}|(z) = |u|_0\left(\frac{z}{L_0}\right) + \frac{|u|_0''\left(\frac{z}{L_0}\right)}{6}\left(\frac{\delta}{L_0}\right)^2 + \ldots + \sigma_u,$$

i.e., the relative error in determining the average velocity profile is:

$$\varepsilon \sim \frac{|u|_0''\left(\frac{z}{L_0}\right)}{6|u|_0\left(\frac{z}{L_0}\right)}\left(\frac{\delta}{L_0}\right)^2.$$

Based on this, we have chosen δ= 6cm, which gives the relative variability (error) of 0.1 for L_0 = 10cm. The same window averaging was carried out for each instant profile. It is seen from Fig. 5 that the averaged temperature and velocity profiles show only a slight variability during a 30 min. intervale. It enables us to use the hypothesis that the random temperature and velocity fields are statistically stationary.

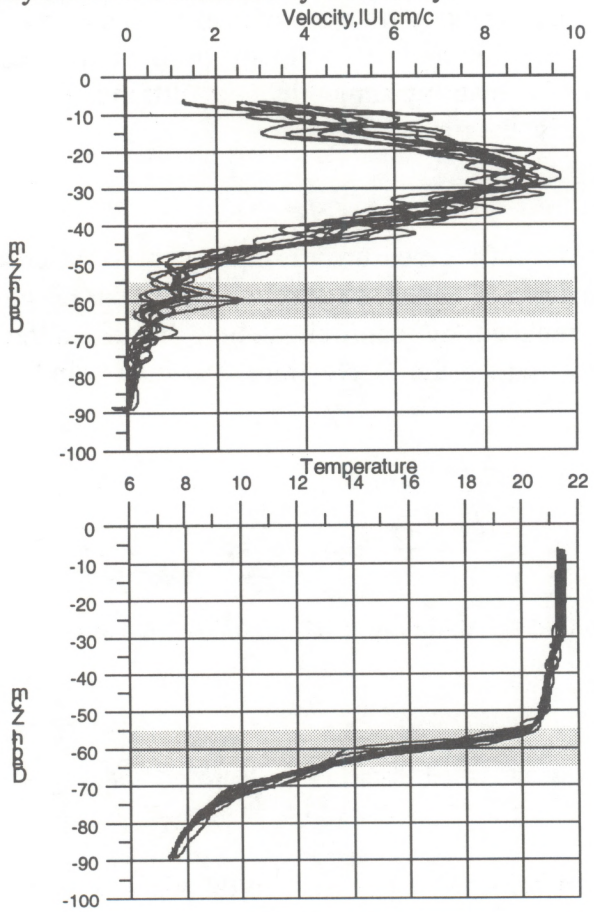

Fig. 5. Window-averaged instantaneous profiles of velocity (above) and temperature (below). The window width is 12 cm.

Before considering the resulting dependencies, let us discuss the meaning of the values obtained upon averaging. We present the instant values of velocity, $\vec{u}$, and temperature t as sums of averaged and oscillating components:

$$\vec{u} = \langle U \rangle \vec{x}_0 + \vec{u}', \qquad (2)$$

$$t = \langle t \rangle + t'.$$

It is obvious from comparison of (2) and (1), that

$$\bar{t}(z) = \langle t \rangle.$$

At the same time, measurements made by the hot-wire anemometer give only an absolute value of the velocity:

$$|u| = \left[\left(\langle U \rangle + u_1' \right)^2 + u_2'^2 + u_3'^2 \right]^{1/2}, \qquad (3)$$

where u_1', u_2', u_3' are the oscillating velocity components. Hence, in general, the averaged absolute value is related to the averaged velocity profile in a complicated manner. For a low turbulence level, when $|\langle U \rangle| >> |u_1'|, |u_2'|, |u_3'|$ it follows from (3), that

$$|u| \cong \langle U \rangle + \frac{\langle u_2'^2 + u_3'^2 \rangle}{2\langle U \rangle}.$$

The dispersion of the velocity fluctuations is as follows:
$\sigma_u^2 = \langle u_1'^2 \rangle$.

But it is obvious from Fig. 4a that the turbulence level in the velocity is not small, so that $\overline{|u|}(z)$ relates to $\langle U \rangle$ in a more complicated way, and $\overline{|u|}(z)$ gives only rough information about the velocity profile. More accurate quantitative estimations of the velocity profile by the same sensors measuring the absolute value of the velocity require reducing the level of turbulent fluctuations. In the present experiment, one can well describe the turbulence only by the temperature fluctuations measured by the electric thermometer.

The obtained profiles $\overline{|u|}(z)$ and *t(z)* were approximated by the following functions

$$t(z) = t_0 + t_z' z + \frac{\Delta t}{2}\left[1 + \tanh\frac{z - z_0^t}{\delta_0^t}\left(1 + \frac{\alpha^t}{\cosh^2 \frac{z - z_1^t}{\delta_1^t}}\right)\right] \text{ and } \qquad (5)$$

$$\overline{|u|}(z) = u_0 + \frac{\Delta u}{2}\left[1 + \tanh\frac{z - z_0^u}{\delta_0^u}\left(1 + \frac{\alpha^u}{\cosh^2 \frac{z - z_1^u}{\delta_1^u}}\right)\right]. \qquad (6)$$

The parameter t_z' determines the temperature gradient within the quasi-homogeneous layers lying above and below the thermocline. It was obtained by the linear approximation of the corresponding pieces of the profile *t(z)*. The parameter t_0 was determined from the known temperature value near the bottom ($t|_{z=-200cm} = 5^0 C$), then

$t_0 = 5^0 + 200 \cdot t_z'$.

Other parameters, $\Delta t, z_0^t, \delta_0^t, \alpha^t, z_1^t, \delta_1^t$ and $\Delta u, z_0^u, \delta_0^u, \alpha^u, z_1^u, \delta_1^u$, were derived by the least square root method.

By using these temperature and velocity profiles, the Richardson number profiles *Ri(z)* were calculated. These profiles for x = 200 cm and different frequencies of rotation of the electric motor are presented in Fig. 6. For U > 40 1/min, the domain of Ri < 1/4 occurs, i.e., the flow could become unstable.

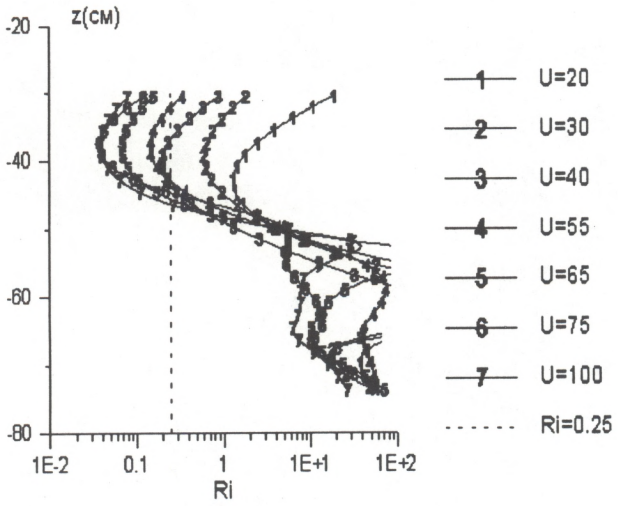

Fig. 6. Profiles of Ri(z) at x = 200 cm, obtained for different angular velocities (frequencies), *U*, of the electric motor rotation (given in 1/min.).

The turbulence spectra are presented in Fig. 7. It is obvious that the spectra of high-frequency oscillations are close to power function with the power index between -3 and -4. Besides one can see a low-frequency peak, which appears at large enough flow velocities (high frequencies of rotation of the electric motor).

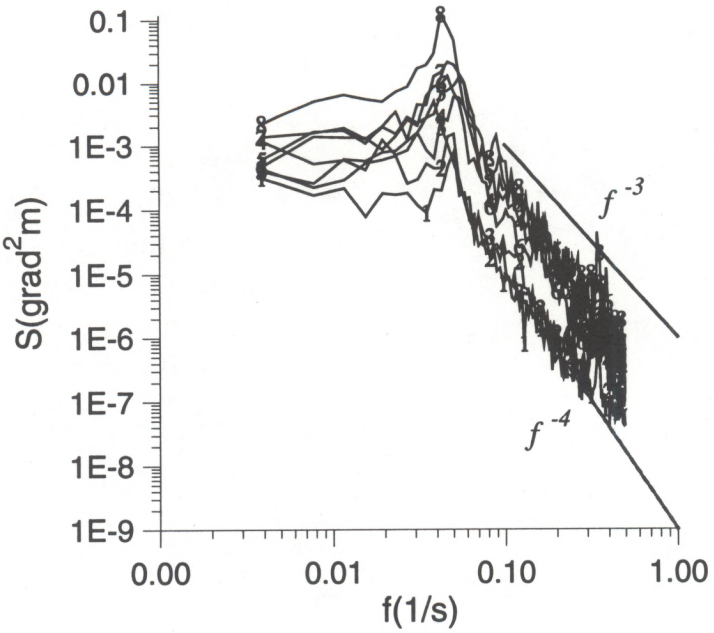

Fig. 7. Spectra of temperature oscillations for different frequencies of rotation of the electric motor (in 1/min).
1) $U = 35$, 2) $U = 40$, 3) $U = 45$, 4) $U = 50$, 5) $U = 55$, 6) $U = 60$, 7) $U = 65$,
8) $U = 75$.

4.2. Study of spatial evolution of a turbulent jet.

Using the temperature and velocity profiles obtained, the dependences of global parameters of the flow and the stratification on the horizontal coordinate x and the initial flow velocity were studied. The velocity and temperature profiles are characterized by their typical vertical scales: the thickness of the shear layer:

$$\delta_u = \int_{-\infty}^{\infty} \left[\frac{1}{4} - \left(\frac{|u|(z)}{\Delta u} \right)^2 \right] dz,$$

the thickness of the thermocline:

$$\delta_t = \int_{-\infty}^{\infty} \left[\frac{1}{4} - \left(\frac{t(z) - t_0 - t_z' z}{\Delta t} \right)^2 \right] dz,$$

and the positions of the "mass centers," z_u and z_t, which characterize the depths of the shear layer and of the thermocline, respectively. These positions can be determined from the following equations:

$$\frac{\delta_u}{2} = \int_{-\infty}^{z_u} \left[\frac{1}{4} - \left(\frac{|u|(z)}{\Delta u} \right)^2 \right] dz,$$

$$\frac{\delta_t}{2} = \int_{-\infty}^{z_t} \left[\frac{1}{4} - \left(\frac{t(z) - t_0 - t_z' z}{\Delta t} \right)^2 \right] dz.$$

The parameters of the above expressions are the total changes (jumps) of temperature, Δt, and velocity, Δu.

At first, the velocity field in the turbulent flow without temperature stratification was studied. The dependences $\delta_u(x)$ for different values of the nozzle output width (i.e., the distance between the lids of the nozzle), D, and the initial flow velocity determined by the frequency of rotation of the flow inductor electric motor, U, are presented in Fig. 8a. The rotation frequency U is used below as a control parameter instead of the flow velocity, because the latter varies essentially in time and space, and, at the same time, the mean flow velocity at a fixed point is proportional to U (see below, Fig. 19). In all cases, the dependence $\delta_u(x)$ can be approximated by the linear function

$$\delta_u(x) = 0.1x.$$

Such a dependence is typical of a turbulent mixing layer. The positions of the mass center z_u and the upper and lower boundaries of the mixing layer, $z_u \pm 2\delta_u$, are plotted in Fig.

8b. It is seen that the deepening of the shear flow and widening of the mixing layer obey the linear laws. The dependence $\Delta u(x)$ is rather irregular and does not satisfy the law $\Delta u \sim 1/\sqrt{x}$ typical of plane turbulent jets. We suppose that it was due to the effect of the water surface. The parameter α^u in (6), which characterizes the deviation of the jet shape from the self-similar one, varied from 0 to -0.5.

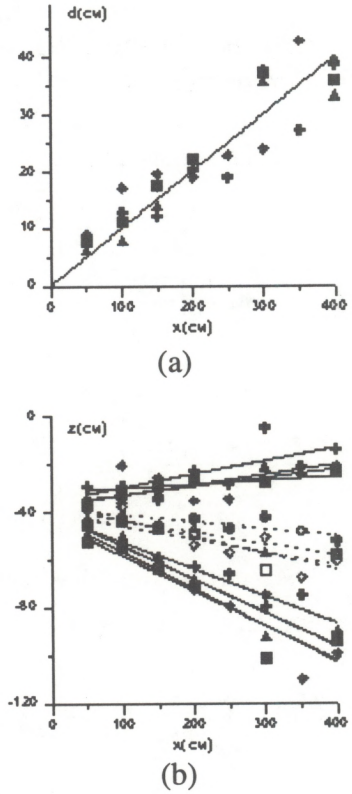

Fig. 8. Geometric parameters of turbulent shear flow without stratification; (a) dependence of the thickness of the shear layer on x, (b) dependence of the center of mass and the boundaries of the shear layer on x. + D = 20 cm, U = 100 1/min;
◆ D = 20 cm, U = 60 1/min; Δ D = 40 cm, U = 120 1/min;
□ D = 40 cm, U = 60 1/min.

Then we studied the parameters of the stratified flow. First, spatial characteristics of temperature and velocity profiles were investigated. The dependencies of the thicknesses of the shear layer and the thermocline on x are plotted in Figs. 9a, 10a, and 11a for stratified shear flows with different initial parameters. The thickness of the shear layer δ_u obviously exceeds the thermocline width δ_t. Besides, δ_u is increasing with x, but δ_t is decreasing with x. The boundaries and the positions of the shear layer and the

thermocline are presented in Figs. 9b, 10b, and 11b. The center of the shear layer is obviously positioned essentially above the thermocline center.

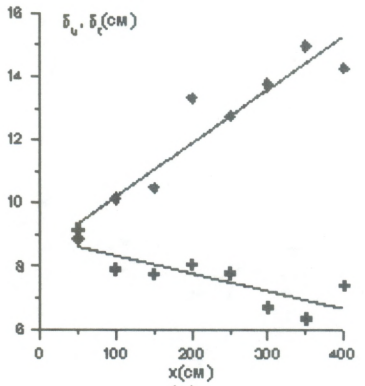

(a)

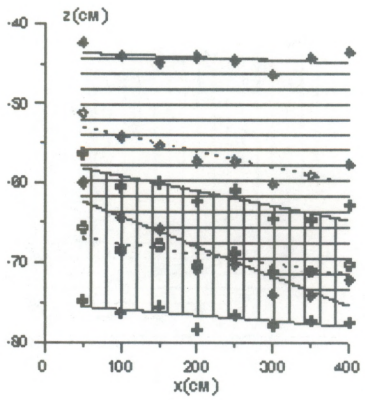

(b)

Fig. 9. Geometric parameters of the stratified shear flow.
D = 40 cm, U = 120 1/min. a) Dependence of the
thickness of the shear layer, ◆, and thickness of the thermocline, +, on x;
b) the depth of the thermocline, ✞ , and of the mixing layer, ◊
and their boundaries, ◆ and + , respectively.

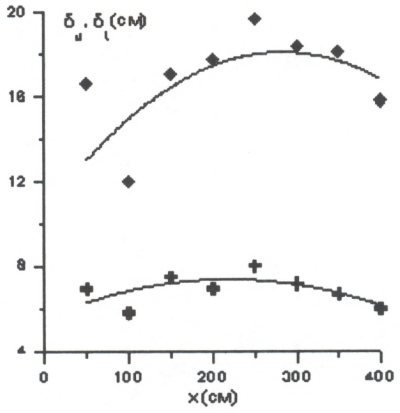

(a)

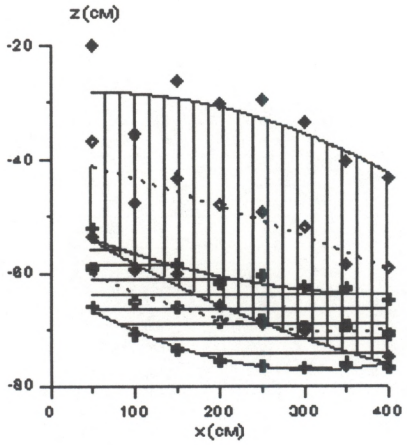

(b)

Fig. 10. Geometric parameters of the stratified shear flow. $D = 20$ cm, $U = 100$ 1/min. a) Dependence of the thicknesses of the shear layer, ◆ , and of the thermocline, +, on x; b) the depths of the thermocline, ✞ , and of the mixing layer, ◊, and their boundaries, ◆ and + , respectively.

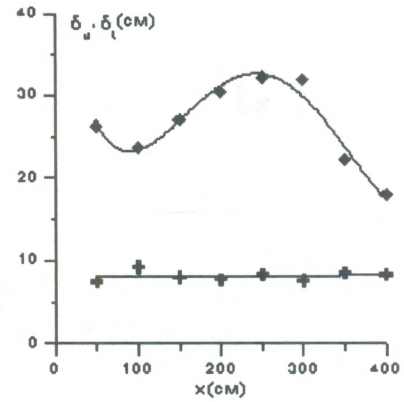

(a)

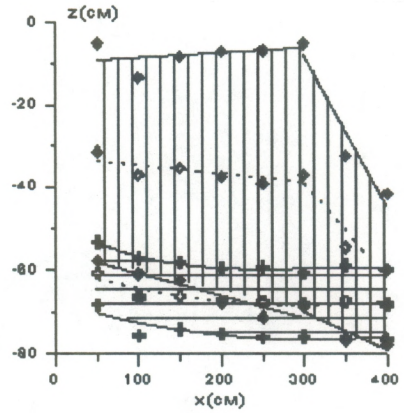

(b)

Fig. 11. Geometric parameters of the stratified shear flow.
D = 20 cm, U = 60 1/min. a) Dependence of the thickness
of the shear layer, ◆ , and of the thickness of the thermocline, +, on x;
b) the depth of the thermocline, ✞ , and of the mixing layer,
◊, and their boundaries, ◆ and + , respectively.

It is well known that the necessary condition of instability of the stratified shear flow is as follows:

$$Ri < \frac{1}{4},$$

where $Ri = N^2 / u_z^2$ is the gradient Richardson number. From the approximations (5) and (6), the profiles $Ri(z)$ for different frequencies of rotation of the electric motor can be determined. The set of these profiles for different x, D = 40 cm, and U = 120 1/min is plotted in Fig. 12. The characteristic feature of the profiles is the domain above the thermocline, where Ri is less than 1/4, i.e. flow can become unstable.

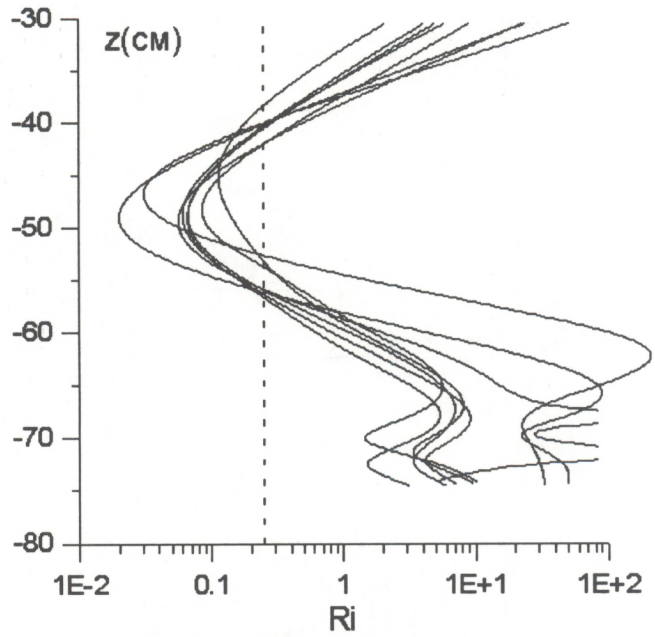

Fig. 12. Profiles of $Ri(z)$ for different x.
$D = 40$ cm, $U = 120$ l/min.

5. Self-oscillations of the turbulent shear flow

If $Ri < 1/4$, the stratified shear flow can become unstable with respect to initial disturbances introduced to the flow due to, for example, vortex shedding from the lids of the nozzle, or vibrations. To study these oscillations, we performed simultaneous records of velocity and of temperature at 14 depths,. The duration of each record was 2048 s.

5.1. Study of the space-time structure of disturbances for different regimes of the flow

First, the "instantaneous" spatial distribution of the temperature was measured. For this purpose, the temperature sensors were towed by the moving trolley. The results of the measurements for the different velocities of the trolley are presented in Fig. 13. It is seen from the figure that there are no significant temperature oscillations at $x > 800$ cm.

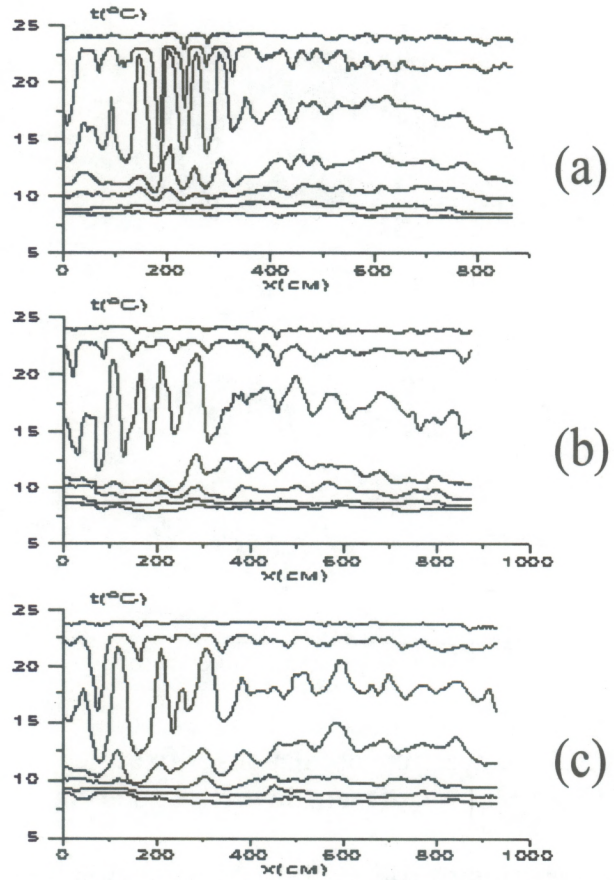

Fig. 13. Spatial variations of temperature measured at different depths for different towing speeds, v, of the bar of electric thermometers
(a) v = 10 cm/s, (b) v = 20 cm/s, (c) v = 30 cm/s

To confirm this result, temperature versus time recordings at 14 depths for x = 200 cm and x = 1000 cm (U = 100 1/min) were performed. These realizations are presented in Fig. 14. It is clear that there are no regular oscillations at x = 1000 cm. Hence, it is possible to conclude that considerable temperature fluctuations occur at x < 800-1000 cm.

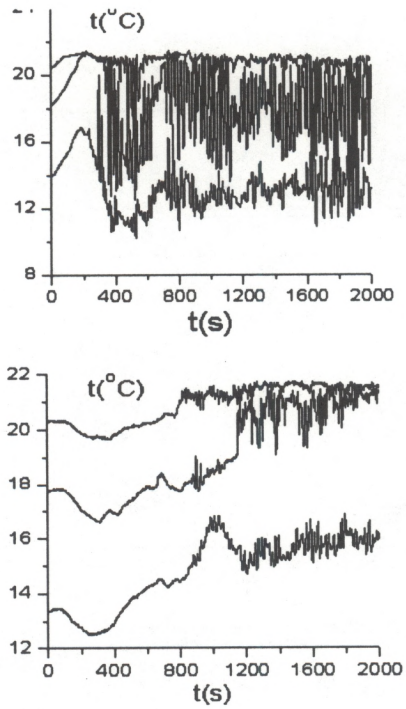

Fig. 14. Temperature oscillations at fixed depths.
Upper plot: x = 200 cm, lower: x= 1000 cm.

5. 2. Spectral characteristics of the excited oscillations for different flow regimes

Using measurement data, the averaged power spectra of temperature oscillations at fixed depths were determined. For this purpose the total time of measurements was divided into 16 intervals containing 128 points each. The power spectra were calculated over these intervals. Then the averaged power spectra, S_t , were calculated as

$$S_t(f) = \sum_{i=1}^{16} S_t^i .$$

The spectra $S_t(f)$ obtained at different distances x from the nozzle for three regimes of turbulent shear flow: D = 20 cm, U = 60 1/min and 100 1/min, and D = 40 cm, U = 120 1/min, are presented in Figs. 15, 16, and 17. The characteristic feature of the spectra is the presence of relatively narrow peaks at the frequency $f \approx$ 0.05Hz (the oscillation period of 20 s). Strong intermittence of dependence of the spectral density on x was observed for D = 20 cm U = 60 1/min (Fig. 16).

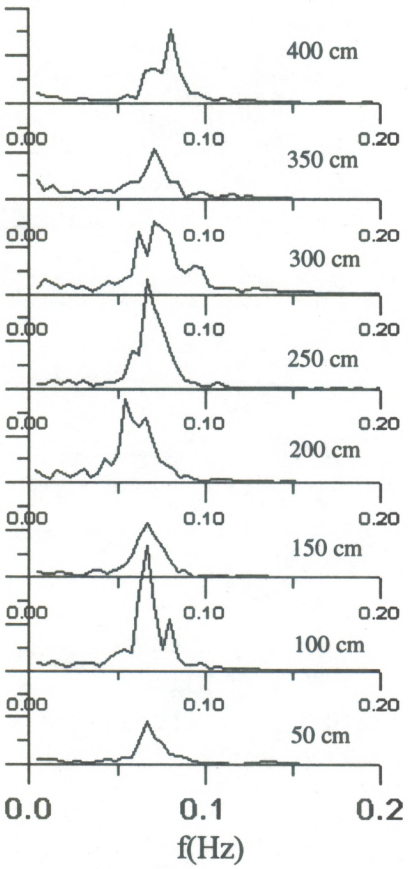

Fig. 15. Spectra of temperature oscillations for different x. $D = 40$ cm, $U = 120$ 1/min.

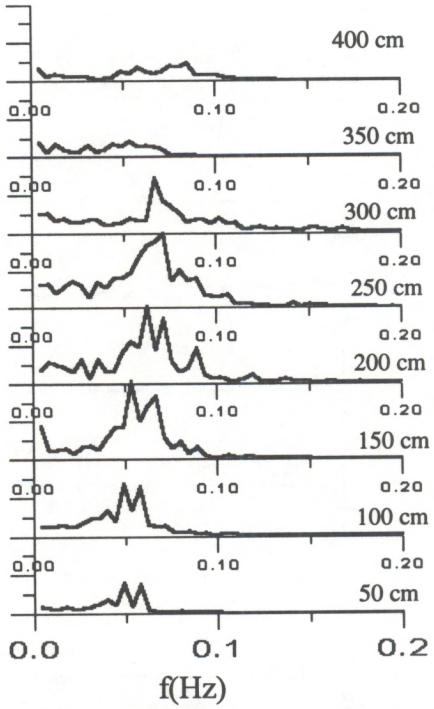

Fig.16. Spectra of temperature oscillations for different x.
D = 20 cm, U = 60 1/min.

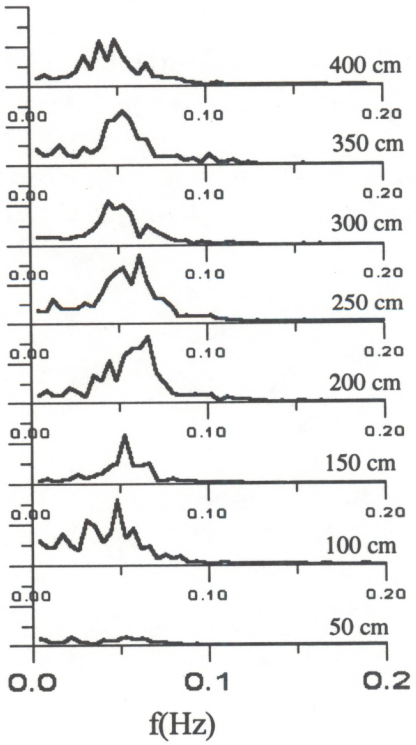

Fig. 17. Spectra of temperature oscillations for different x.
D = 20 cm, U = 100 1/min.

The spectra of temperature oscillations at different depths are presented in Fig. 18 for D = 40 cm, U = 120 1/min and x = 200 cm. It is seen that narrow spectra exist within the thermocline, where the local buoyancy frequency exceeds f.

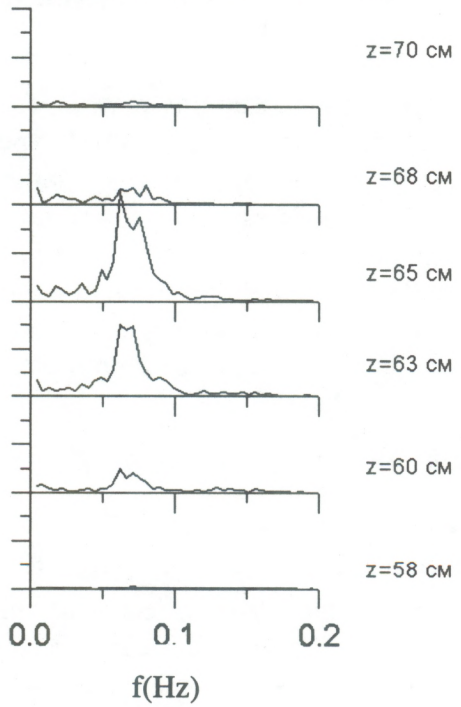

Fig. 18. Spectral density of temperature oscillations at different depths. D = 40 cm, U = 120 1/min, x = 200 cm.

5. 3. Convective and absolute instability of shear flows

Before discussing the experimental results, we will briefly consider the concepts of the convective and absolute instabilities and the local and global instabilities in shear flows. Recently these concepts were discussed in connection with the fluid flow stability (Huerre and Monkewitz, 1985, 1990; Monkewitz, 1990). These concepts were first introduced in electronics and plasma physics by Sturrock, Briggs, and others (see, e.g., Briggs, 1964).

The concepts of convective and absolute instabilities are introduced when considering the linear evolution of finite-length wave trains. Such wave trains, in general, diverge upon propagation. When the medium is not in equilibrium, these disturbances can grow. The instability is called absolute if, in spite of the motion of the wave train, the disturbance grows to infinity in each point of the considered spatial interval. If the wave train is translated so fast that the disturbance in each fixed point of the space tends to zero when $t \to \infty$, then the instability is called convective.

If the complex dispersion relation of the system is $\omega = \omega(k)$, then the stability criterion determining the type of instability is as follows (Briggs, 1964). If k_0 is the wave number for which

$$\left.\frac{d\omega}{dk}\right|_{k=k_0} = 0,$$

then the instability is absolute, if $\mathrm{Im}[\omega(k_0)] > 0$, and it is convective, if $\mathrm{Im}[\omega(k_0)] < 0$.

In general, the character of the instability may depend on the frame of reference. Hovewer, distinguishing between two aforementioned types of instability still makes sense with respect to a preferred, laboratory reference frame that can be determined in most practical cases. This distinction is especially important when the flow parameters are slowly varying in the longitudinal direction. As shown in Monkewitz (1990), the self-oscillations can be excited under such conditions. In hydrodynamics these oscillations are called globally unstable. In the case of weak super-criticality (i. e., close to the self-excitation threshold), the amplitude of a globally unstable mode obeys the Ginsburg-Landau equation (Monkewitz, 1990):

$$\frac{dA}{dt} = [\sigma_r + i\sigma_i](R)A - (l_r + il_i(R))|A|^2 A + \beta \qquad (7)$$

Here R is a control parameter, σ_r is the linear growth rate, σ_i is the frequency of oscillations, l_r, l_i are nonlinear additions to the damping rate and frequency, respectively, and β is the external forcing, which models the effect of turbulent fluctuations in the flow. The examples of such self-oscillations are Karman vortex shedding, which is an example of the absolute instability of the wake behind a two-dimensional bluff body (Monkewitz and Nguyen, 1987), instability of a capillary jet (Leib and Goldstein, 1986), and instability of a low-density heated jet (Monkewitz and Sohn, 1986).

Three criteria of excitation of a globally unstable mode in the system were formulated by Huerre and Monkewitz (1990). The first one is the existence of a narrow frequency spectrum. This is, however, not a reliable criterion of a global mode excitation, because the disturbances in a convectively unstable system may possess the same narrow spectrum. The second criterion of the globally unstable mode excitation is manifested as a response of the system to the external forcing. If a global mode is excited in the system, far enough from the excitation threshold, the amplitude of the output motion should not depend on the amplitude of the external forcing. If there are no global mode excited in the system, the output signal amplitude grows with the amplitude of the external forcing. This criterion is not quite reliable in our case either, because under the conditions of weak supercriticality, the amplitude of the output signal still depends on the external forcing.

The third criterion of the global mode excitation is the typical dependence of the amplitude of the stationary wave disturbances on the control parameter, which follows from the Landau equation. In the problem under consideration, the control parameter R is chosen to be the frequency U of rotation of the electric motor. If U exceeds a critical value U_c, then $\sigma_r > 0$, and oscillations are excited in the system. If $|U - U_c| << U_c$, then the dependence of amplitude of the stationary oscillations is as follows

$$\alpha(U - U_c)A - \gamma A^3 + \beta = 0, \qquad (8)$$

where γ is the nonlinear damping.

When we studied the excitation of oscillations in the large thermostratified tank, we checked the first and the third criteria (see below).

5.4. Discussion of experimental results

A narrow peak was observed in the spectra of oscillations, but, as emphasized in Huerre and Monkewitz (1990), this criterion is not very reliable, so the third criterion was verified. According to Huerre and Monkewitz (1990) the steady amplitude of the global mode A obeys Eq.(8).

To check (8), the temperature oscillations were measured for different rates of rotation of the electric motor U that are proportional to the flow velocity. It is obvious from Fig. 19 that the maximum velocity value at the axis of the jet Δu (see (6)) is proportional to U.

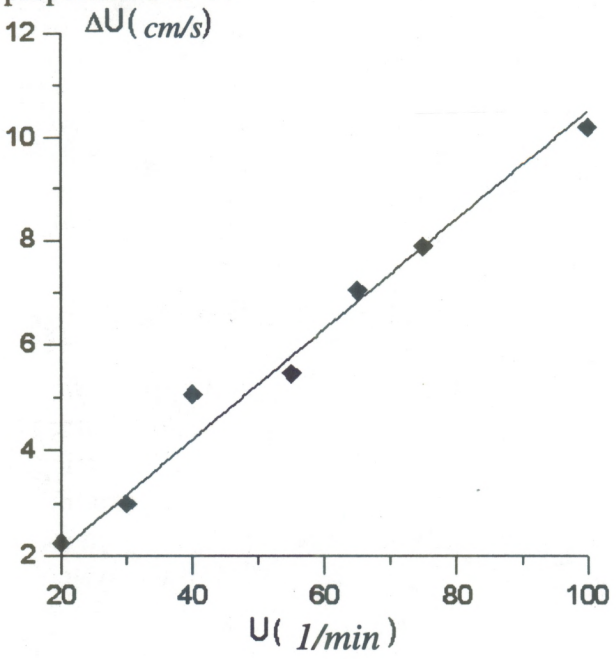

Fig. 19. Dependence of maximal velocity at the axis of the turbulent flow on the frequency of rotation of the electric motor of the flow inductor. The distance from the output block is $x = 200$ cm.

The spectra of temperature oscillations for different rotation frequencies are shown in Fig. 20. It is seen that the narrow peak appears when U exceeds 65 1/min.

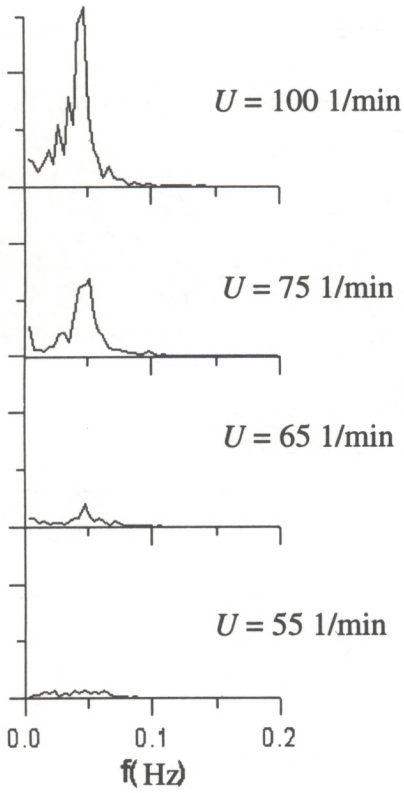

Fig. 20. Spectral density of temperature oscillations for different frequencies of rotation of the electric motor (x= 200 cm, D = 20 cm).

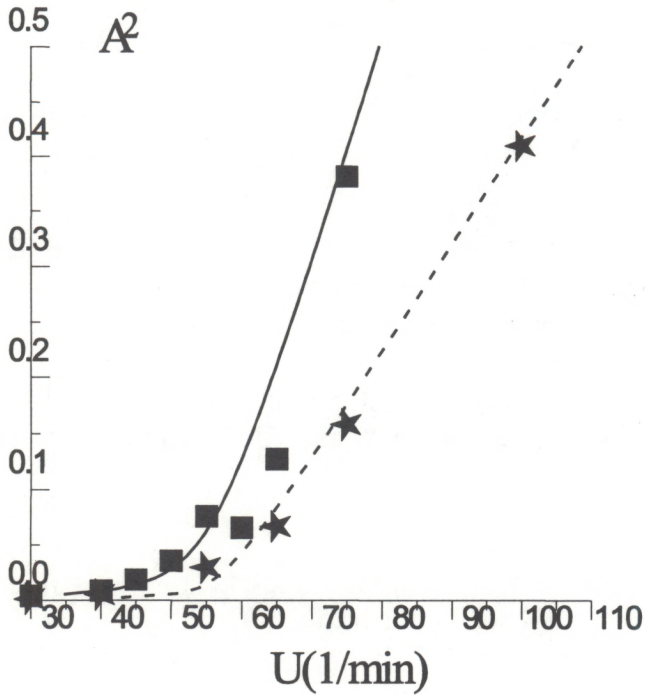

Fig. 21. Dependence of the square of the temperature oscillation amplitude on the frequency of rotation of the electric motor of the flow inductor
■ - experiments with the grid at the inductor output, ★ - experiments without a grid. Solid and dashed curves present the respective dependencies $\alpha(U-U_c)A-\gamma A^3+\beta=0$, where parameters α and β are determined by the best-fit condition.

The amplitude of quasi-harmonic oscillations at the frequency corresponding to the spectral peak was found. It was defined by the following integral:

$$A^2=\int_{f_0-\delta f}^{f_0+\delta f} S_t(f)df,$$

where δf was chosen as equal to one-half of the width of the peak (approximately 0.015 Hz). The experimental points were plotted in the plane (A^2,U). In Fig. 21 there are two different sets of the experimental points corresponding to two experiments. To reduce turbulent fluctuations, we have put a grid near the nozzle. At first the measurements were carried out without the grid, then with the grid. Then α, β, and γ were obtained by the least squares method for both cases. The corresponding lines are presented in Fig. 21. The lines obviously fit the experimental points well. It agrees with the hypothesis of excitation of the global mode in the tank. When U is not very close to U_c, A depends on U as a typical square root function

$$A=\sqrt{U-U_c}. \qquad (9)$$

It follows from Fig. 21 that the critical rotation frequency of the electric motor U_c is approximately 54 1/min, which is in good agreement with the appearance of the spectra in Fig. 20, when the narrow peak arose for U > 60 1/min. According to Huerre and Monkewitz (1990), the existence of these dependencies is the reliable indirect criterion of the global mode excitation. It should be noted, that the narrow spectral peak corresponding to the excited oscillations is less pronounced as the system is too close to the excitation threshold. In this case, the oscillations (which are, naturally, weak) have a considerable spatial variability (see Fig.16, where U is only slightly above the threshold value of about 54 1/min.).

5. 5. On the explosive instability of shear flows

The problem of linear stability of shear flows with given velocity and density profiles is commonly solved in the framework of the eigenvalue problem for the Taylor-Goldstein equation (e.g., Gossard and Hooke, 1975). As previously mentioned, the necessary condition of instability is Ri < ¼, which is fulfilled for the area above the thermocline in the large tank (e.g., Fig. 12). If $\psi=A\varphi(z)e^{i(kx-\omega t)}$ is the stream function disturbance, the instability exists if the eigenvalue ω of the boundary problem for the function φ(z) is imaginary. In a purely linear description, this means exponential growth of the perturbation. When nonlinear effects are taken into account, this exponential growth may be saturated up to the establishment of oscillations with a constant

amplitude. However, in other cases different wave modes can interact resonantly, if the resonance conditions are fulfilled; namely, for one-dimensional processes, the relations $k_1+k_2=k_3$ and $\omega_1+\omega_2=\omega_3$ must be fulfilled simultaneously. In passive systems, these resonant interactions yield just an energy exchange between these waves. However, in the presence of a flow, all three modes can grow in time (in case one of them is the so-called wave of negative energy, see, e.g., Ostrovsky et al., 1986). This growth is, in general, non-exponential, and may have "explosive" character, when the wave amplitude grows infinitely during a finite time interval (Voronovich and Rybak, 1978; Voronovich et al., 1980; Moiseev et al., 1983, 1984, 1986). Interactions of the boundary modes (having wave numbers lying at the boundary of linear stability) are the fastest ones among all known explosive interactions (Moiseev et al., 1983, 1984, 1986). The explosion time of such disturbances, t_0, is of order $\varepsilon^{-1/2}$, where ε is of the order of the dimensionless wave amplitude. At the same time, the time of explosion for the non-boundary modes (Voronovich and Rybak, 1978; Voronovich et al., 1980) is of order ε^{-1}.

A simple model of the stratified shear flow, which enables one to explain the main features of the explosion resonance interaction of boundary modes, the Kelvin-Helmholtz flow, was considered by Moiseev et al. (1983, 1984, 1986). It is a two-layer flow of different density fluids in the gravitation field with the tangential jump of velocity and surface tension at the layer interface. In the Lamb's reference frame, when $\rho_1 U_1+\rho_2 U_2=0$ ($\rho_{1,2}$ and $U_{1,2}$ are densities and velocities of the upper and lower layers), the dispersion relation for the linear eigenvalue problem in the dimensionless variables normalized by the space scale, $l_0=(\sigma/g(\rho_2-\rho_1))^{1/2}$, and the time scale, $t_0=(l_0[\rho_1+\rho_2]/g[\rho_2-\rho_2])^{1/2}$, is as follows:

$$D(\omega,k)=\frac{\omega^2}{k}-k^2-1+\langle U^2\rangle k=0,$$

where $\langle U^2\rangle=(\rho_1U_1^2+\rho_2U_2^2)/(\rho_1+\rho_2)$ is the parameter of stability of the flow.

The plane of parameters $(\langle U^2\rangle,k)$ can be divided into domains of growing and neutrally stable disturbances by the boundary curve $\langle U^2\rangle=k+\frac{1}{k}$, corresponding to $\omega=0$. In the unstable region, the classical Kelvin-Helmholtz instability occurs. The explosion is possible for resonantly interacting modes whereas, as mentioned above, the most intensive growth corresponds to boundary modes. In the case considered, the above resonance conditions are fulfilled, in particular, for two boundary modes with $\omega(k_1)=\omega(k_2)=0$ if their wave numbers, k_1 and k_2, are such that $k_1=2k_2$; this case is realized when $\langle U^2\rangle=3/(2)^{1/2}$.

A standard way to describe the behavior of perturbations is to introduce a "slow" dependence of the amplitude, A, on time, and write the coupled equation for A. In "ordinary" cases, these equations are first-order each, but for the boundary modes the coefficients at the first time derivatives that are proportional to $m_1=\partial D(\omega,k)/\partial\omega=0$,

turn to zero, and the equations for the wave amplitudes are second-order each, which provides faster growth as mentioned before. In the two-layer case considered, the amplitudes of the first and second spatial harmonics, $A_1(\tau)$ and $A_2(\tau)$, are as follows:

$$\frac{1}{k_1}\ddot{A}_1 = qA_2A_1^*; \frac{1}{k_2}\ddot{A}_2 = \frac{1}{2}qA_1^2; q = \frac{3}{\sqrt{2}}\frac{\rho_2 - \rho_1}{\rho_2 + \rho_1}, \qquad (10)$$

where dots mean derivatives with respect to $\tau = \sqrt{\varepsilon}t$. These equations have a self-similar solution:

$$A_2 = A_1 \frac{6}{k_1 q(\tau_0 - \tau)^2},$$

which tends to infinity at the finite time

$$\tau_0 = \sqrt{6/qk_1A_0},$$

where $A_0 = A_1(0) = A_2(0)$. Numerical calculations show that for all initial conditions, the solution tends to the self-similar one.

In shear flows with continuous profiles of velocity and density, the coefficient m_1 at the first derivative in the amplitude equation for boundary modes is determined as follows (Engevik, 1982):

$$m_1 = \frac{I_1}{I_0},$$

$$I_0 = \int_{z_1}^{z_2} \varphi^2 dz; \qquad I_1 = \int_{z_1}^{z_2} \left[\frac{2N^2}{(U-c)^3} - \frac{U''}{(U-c)^2} \right] \varphi^2 dz.$$

Here $c = \omega/k$, $U(z)$ is the undisturbed velocity profile, $N(z)$ is the Brunt-Vaisala frequency, and z_1 and z_2 are the lower and upper coordinates of the total fluid layer. Note that the integral I_1 is proportional to the adiabatic invariant density over the unity of the horizontal surface, determined in Engevik (1982) for the real eigenfunctions $\varphi(z)$.

The integral I_1 enables one to determine the flows, for which the coefficient m_1 equals to zero, i.e. there is the strongest explosive wave interaction. It is shown in Moiseev et al., (1984), that such a possibility can be realized in the stratified plane Couette flow, which is a two-dimensional flow with the linear Brunt-Vaisala frequency profile and the linear velocity profile between two horizontal planes. In variables normalized by the distance between the planes, $2L$, and by the velocity at the upper plane, U_0, the velocity profile of the undisturbed flow is a follows:

$U = z$ for $-1 < z < 1$, $N^2 = z^2$.

The amplitudes of resonant boundary modes obey the following equations:

$$\ddot{A}_1 = -q_1A_2A_1^*; \ddot{A}_2 = -q_2A_1^2,$$

which coincide with (10) when substituting $A_2 \to -A_1$. Consequently, they have the same self-similar explosive solutions.

In real systems, the explosive growth (as well as the exponential one) will be eventually restricted by additional factors, such as strong nonlinearity or wave breaking with the formation of turbulence. Thus, it seems most productive to investigate the global behavior of self-oscillation in the shear flow, as described above.

6. Conclusions

The above material described the observation of oscillations excited in a turbulent stratified shear flow in a large thermostratified tank with a specially designed flow inductor. These oscillations arise when the flow velocity exceeds some critical value. Since the flow velocity varies considerably along the tank, the frequency of rotation of the electric motor of the flow inductor, which creates this flow, was taken as a control parameter. The waves occur when the rate of the electric motor rotation exceeds 54 1/min.

There appears to be a narrow peak in the spectrum of the generated waves with a peak frequency of about 0.05 Hz and width, at the 0.5-level, of 0.015 Hz. The amplitude of the oscillations corresponding to this peak depends on the control parameter in accordance with (9), where U_c = 54 1/min.

These two criteria (the narrow spectrum and the square-root dependence of the amplitude on the control parameter) were determined in Huerre and Monkewitz (1990) as two of three main criteria of excitation of a global mode in the system.

To explain the observed effect of generation of oscillations in the flow, one should elucidate the mechanism of positive feedback which is necessary for transferring from spatial amplification to the generation of a global mode. Two variants are possible depending on the character of local instability of the stratified shear turbulent flow. If there is convective instability, then the globally unstable mode can be realized only due to wave reflection from the construction features of the tank (for example, from its end wall or the water intake end of the flow inductor). Another possibility can be realized if there is absolute instability in the shear flow. In this case, the global instability can occur due to an internal feedback, without any reflections. The following fact confirms the latter mechanism. As mentioned above, the oscillation amplitude decreases rapidly with the distance, x, from the nozzle, and there are practically no oscillations near the water intake part of the inductor, hence no reflections.

The observed process can be interpreted as generation of three-dimentsional internal waves by the flow. For that, the phase velocity of the wave should be oriented in the flow direction. As known from the electromagnetic analogs, due to the wave drift on the flow, its group velocity can be directed opposite to the phase velocity, so that the wave energy returns to the flow output, thus securing the internal feedback and yielding the absolute instability. Such a possibility can be realized in oceanic currents, wakes, etc. This hypothesis warrants further investigation.

Part 2: Modulation of Nonlinear Surface Waves by an Internal Wave

1. Introduction

Preliminary experiments in the oval wind-wave tank included:
- Creation of two-layer density stratification by salt and excitation of internal gravity waves by a wave maker.
- Measurements of capillary-gravity waves by a laser slope gauge. Retrieval of frequency spectra of capillary-gravity waves.
- Modelling of modulation of "parasitic" capillary ripples on the slopes of regular gravity waves due to internal waves.

2. Creation of density stratification by salt and excitation of internal gravity waves by a wave maker in an oval wave tank

2.1. Density stratification

The oval wind-wave tank is a closed tank with two straight-line operating sections 2.4 m long and two semicircular sections with a 1.9 m radius. The total height of the tank is 0.59 m, the width is 0.29 m, and the maximum water depth in the hydrochannel is 0.3 m. The continuation of one of the operating sections is an auxiliary section 1.2 m long with an internal wave (IW) generator mounted in it. For a more detailed description of this facility see one of the previous ETL Memorandums (Bogatyrev et al, 1997).

The stratification in the oval wave tank was created by using a salt solution fed under the water layer, from a reservoir placed above the tank. The solution delivery speed was controlled in order to avoid strong mixing near the interface, so that the density stratification in the experiments corresponded to upper and lower homogeneous layers with a thin intermediate layer with a strong density gradient. Usually it took 5 to 8 hours to create the salt stratification in the tank. Typical resulting density differences between the lower and upper layers were about 0.025-0.04 g/cm^3. The upper and lower layer depths were about 12-13 cm, with an intermediate layer depth of 3-4 cm. Time evolution of stratification profiles has been studied using the conductivity probe, which was also used for measurements of internal waves. Figure 22 presents stratification profiles measured in the course of one set of experiments.

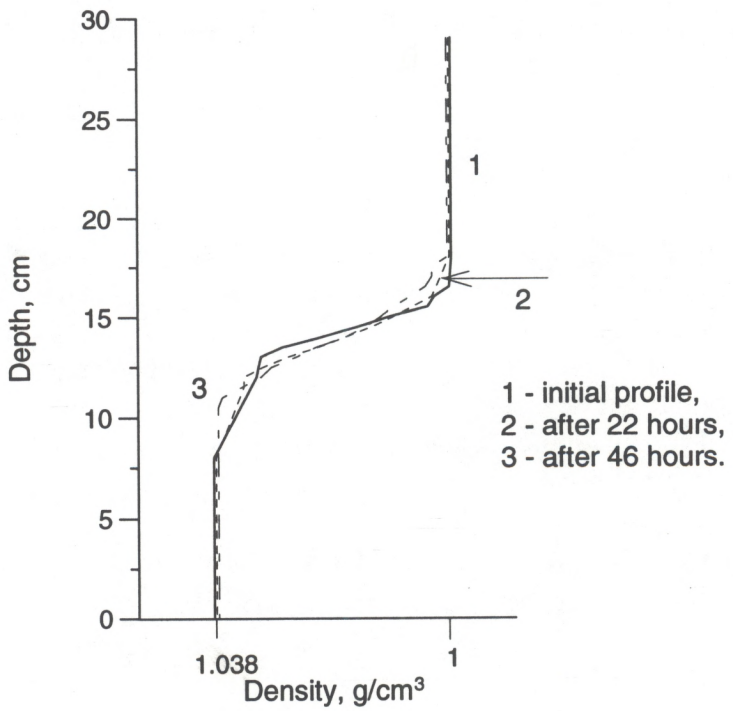

Fig. 22. Profiles of salt stratification in the oval wave tank.

The first profile in Figure 22 was measured before the experiments, two other profiles were measured after 22 hours and 46 hours, respectively. Note that the second and third profiles were measured after experiments in which the internal waves generator was working for 1 to 2 hours. One thus can conclude that the stratification is quite stable and is not changed significantly as a result of diffusion and turbulent mixing of the interface produced by the wave generator.

2.1. Excitation and measurements of internal gravity waves

The IW generator in the wave tank is a vertical blade 23 cm high oscillating around the middle horizontal axis (see Fig. 23) and driven by a DC motor. The oscillation amplitude of the blade is controlled by an eccentric, while the frequency by the motor voltage. The characteristic IW periods were within 8.5-10 s and the IW amplitudes varied in the range 0.2-1.5 cm.

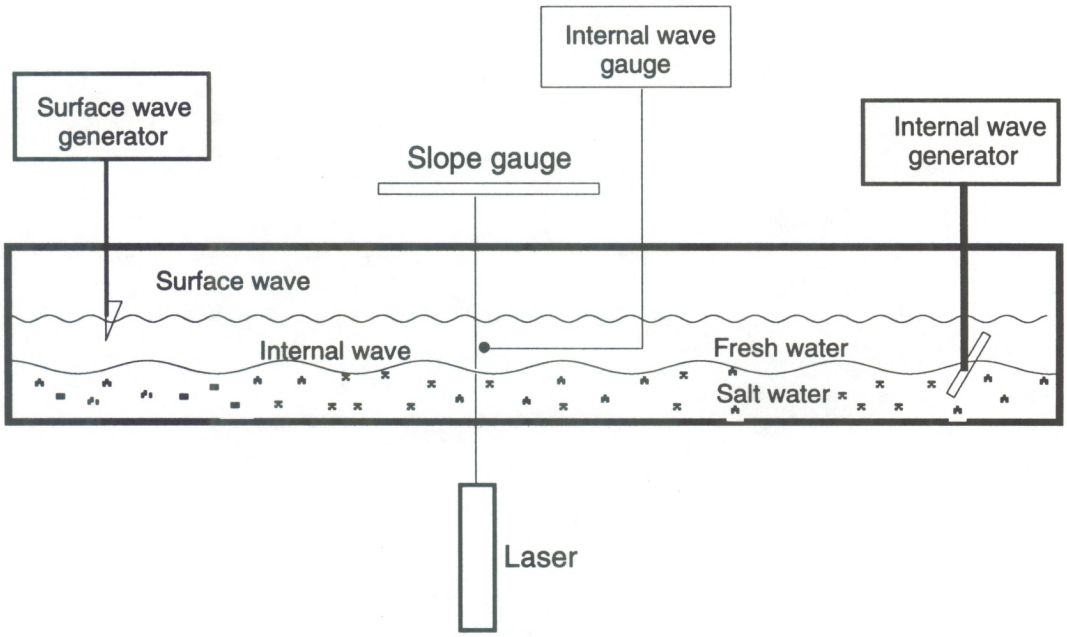

Fig. 23. The experimental setup for IW-SW interaction investigation.

Internal waves were measured by a wire resistance-type wave gauge. The gauge was installed approximately at the depth of the interface. The gauge allowed us to measure IW of amplitudes larger than 0.5-1 mm. Mechanically generated internal waves were absorbed in the second circular section of the oval wave tank. The absorber consisted of thin plastic stripes hung vertically at special frames, spaced at 5 -10 cm, the total number of the frames was 12. Although IW are damped by the absorber quite effectively, there are some reflections from the absorber, and also a train transmitted through it and returning to the gauge (even before the reflected wave) because the tank is closed. Figure 24 shows a short internal wave train generated by the wave maker and corresponding transmitted (t) and reflected (r) wave trains. The latter are small compared to the initial internal wave: the reflection and transmission coefficients are less than 10%. Thus, one can approximately consider the main IW train as a progressive wave.

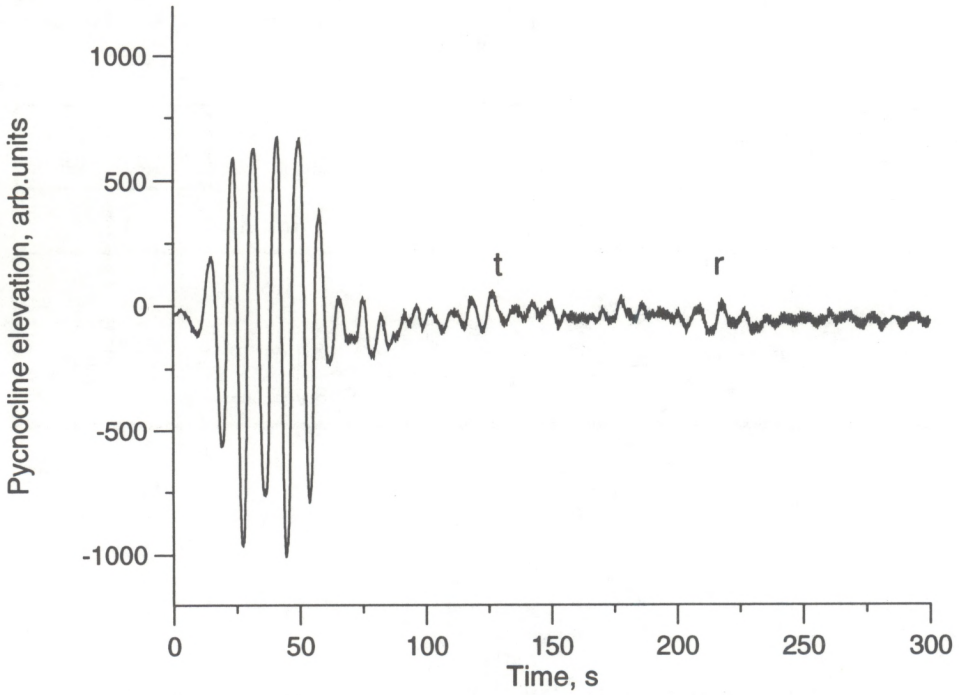

Fig. 24. A record of a mechanically generated internal wave train in the oval wave tank; (t) and (r) denote transmitted and reflected internal waves.

3. Excitation and measurements of gravity-capillary waves (GCW)

The generator of surface waves (SW) is a vertically oscillating quarter cylinder driven by a DC motor. The amplitude and frequency of the oscillations are controlled in a similar way as the IW. The characteristic frequencies used in our experiments were 4-5 Hz, the maximum oscillation amplitude was 3 mm. For steep SW in this frequency range the mechanism of excitation of parasitic ripples is the most effective. The SW generator could be placed at any point in the tank. In the experiments on internal wave/surface wave interaction, the SW generator was installed in the first straight section of the tank.

Surface waves were measured using a laser slope meter. The laser slope meter included a laser mounted under the tank bottom with the laser beam directed vertically upwards and was recorded by a system placed above the tank (see Figure 23). The receiver is a photosensitive strip, so that the slope meter measures wave slopes only in one direction; to average laser beam oscillations in the transverse direction, the beam was transformed into a "knife" beam by using a cylindrical lens. The slope meter can measure slopes of waves with the frequencies of the order of 200 Hz and less. The slope meter response as a function of the beam coordinate on the strip is shown in Figure 25, nonlinearity of the slope meter is about 1%.

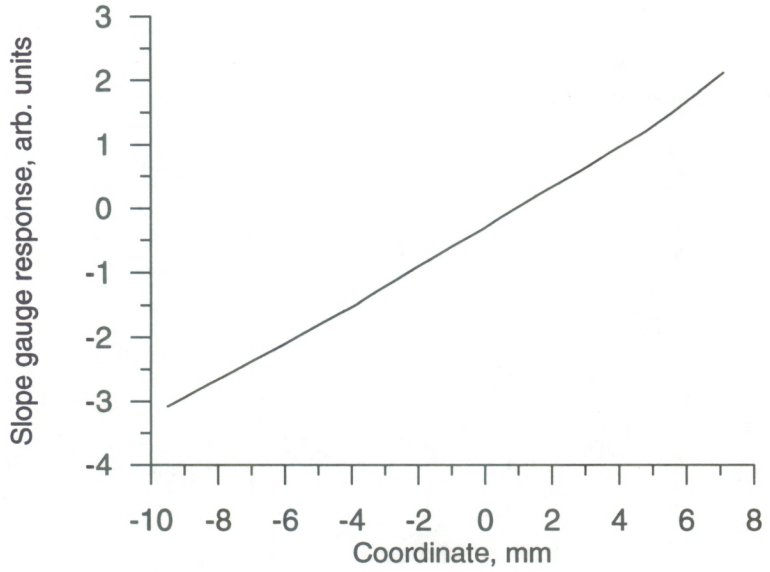

Fig. 25. Slope gauge response vs. laser beam coordinate on the photosensitive strip.

Measurements of elevation of the water surface due to GCW were also carried out using a resistance-type wire gauge. The measurements were simultaneous and nearly collocated with the slope measurements.

Examples of GCW slope profiles obtained by the slope meter are shown in Figure 26 for two different amplitudes of surface waves, corresponding to the amplitudes of SW generator 0.5 mm and 2mm, respectively. Parasitic capillaries generated by steep GCW are clearly seen at the profile of the basic short gravity waves.

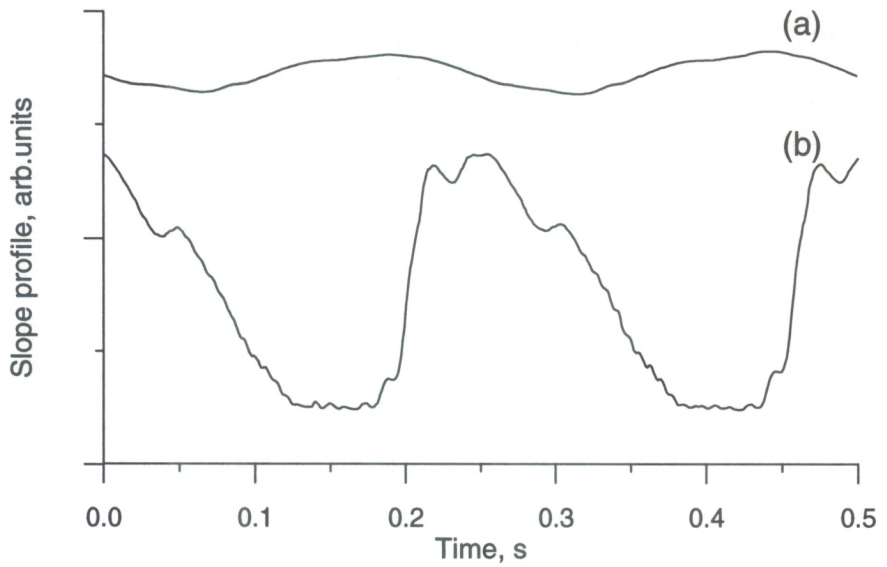

Fig. 26. Slope profiles of surface waves of low amplitude (a) and of high amplitude (b).

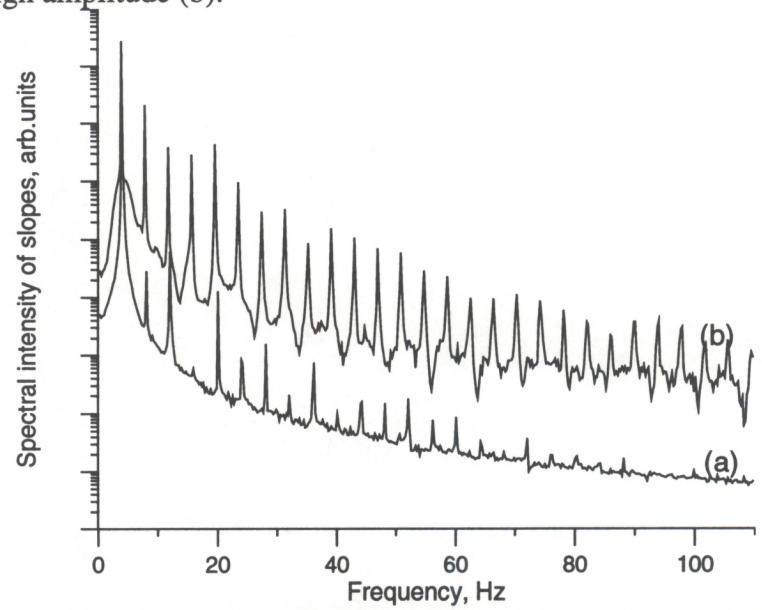

Fig. 27. Spectra of regular surface waves of low amplitude (a) and of high amplitude (b), corresponding to the profiles in Fig. 26.

Figure 27 shows the frequency spectrum of mechanically generated quasi-monochromatic SW ("regular SW"), corresponding to the low and high wave amplitudes in Figure 26. The steep SW are characterised by numerous high-order harmonics in the spectrum, and the generation of the parasitic ripples, in particular, is manifested as nearly a "plateau" of the spectrum envelope at frequencies of about (40-50) Hz. This is in agreement with previous measurements (see Ermakov et al.,1986; Perlin et al., 1993).

A dependence of the intensity of a high-order harmonic on amplitude of the main harmonic of basic GCW is illustrated in Figure 28.

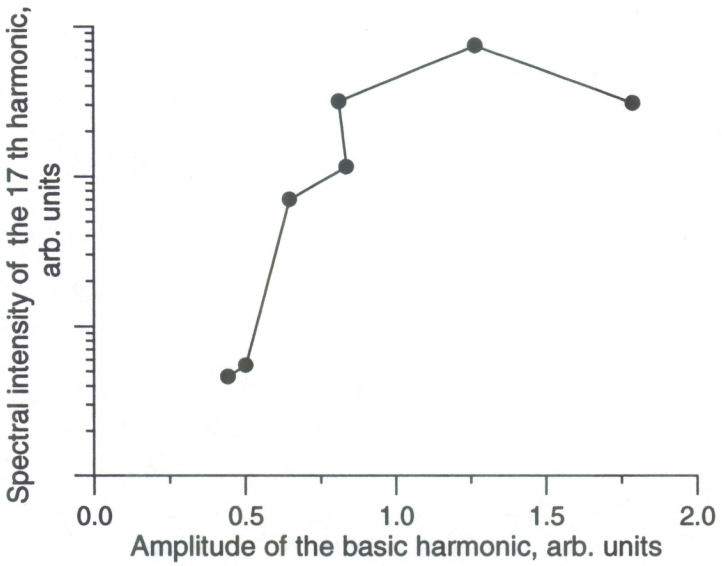

Fig. 28. Intensity of a high-order harmonic as a function of the elevation amplitude of the basic harmonic of GCW.

It is clearly seen that the intensity of high-order harmonics (in particular, those corresponding to frequencies of parasitic ripples) increases sharply in the vicinity of "critical" amplitude of GCW. This peculiarity forms a base for the studied "cascade" modulation of short surface waves due to IW. Some results of these studies are presented in the following section.

4. Observation of strong ("cascade") modulation of "parasitic" capillary ripples due to internal waves

Up to now two main physical mechanisms of IW/SW interaction were studied in the literature: hydrodynamic modulation of SW due to nonuniform currents induced by IW ("kinematic" mechanism) and modulation of SW due to redistribution of surface films by IW ("film" mechanism, see, e.g., Basovich et al., 1982 and Ermakov. et al., 1982, respectively). The "kinematic" mechanism is known to be the most effective in case of resonance, when the phase velocity of internal waves is close to the group velocity of surface waves. The kinematic modulation of SW was studied in wave tank experiments by Lewis et al. (1974), and by Ermakov and Salashin (1984). Here we study another modulation mechanism, based on the assumption that the basic gravity-capillary waves generate high-order nonlinear harmonics ("bound" waves), in particular, "parasitic" capillary ripples, and that the modulation of the basic waves leads to modulation of the bound waves. Since the intensity of the "parasitic" ripples depends nonlinearly on the amplitude of the basic GCW, as shown in the previous section, one can expect that modulation of these harmonics can strongly exceed the modulation of basic GCW. Testing this hypothesis is the main objective of our experiments.

4.1. Experiments

In the experiments we observed the "cascade" modulation of the "parasitic" capillary ripples (mm-scale bound waves) under the conditions when the basic decimeter-scale GCW were modulated due to the kinematic mechanism. In order to avoid modulation of GCW due to the "film mechanism," the water surface in the experiments was cleaned carefully by wind blowing and by skimming to remove surfactants and thus to exclude the film mechanism of the SW modulation due to internal waves.

Modulation of bound waves was studied for two different amplitudes of internal waves over a wide range of surface wave amplitudes (see Table 1). The experiments were carried out mostly for GCW and IW propagating in the same direction. Some experiments when the waves propagated in the opposite directions showed similar results. The amplitudes of GCW varied from very small values when high-order harmonics were practically absent in the GCW spectrum to large amplitudes with strong nonlinear harmonics in the spectrum. Note that the amplitudes of parasitic capillaries increase most strongly when GCW amplitudes are close to some critical values (see, Ermakov et al., 1986), so that the strongest ripples modulation is expected for these GCW amplitudes.

Table 1. Experiments on "cascade" modulation.

Experiment N	IW amplitude	Amplitude of GCW generator (mm)	Propagation direction of IW and GCW
I	2 mm	0.8; 1.0; 1.2; 1.5; 2.0	parallel
II	4 mm	0.8; 1.0; 1.2; 1.5; 1.8	parallel

IW period in all the experiments was 9.8 s, GCW frequency of about 4 Hz.

4.2. Results and discussion

Figure 29 presents an example of simultaneous records of pycnocline elevations due to internal waves and surface wave slopes recorded by the laser gauge. From the slope record the modulation of the basic GCW with the IW period is clearly seen (this modulation was studied earlier by Ermakov and Salashin, 1984). Also, it is seen that high

frequency ripples are strongly amplified when the basic GCW increases (over IW crests) and practically disappear over IW troughs where the basic wave decreases. This case corresponds to the amplitude of basic GCW close to the critical GCW amplitudes when the "parasitic" ripples generation starts. The frequency spectra of these GCW over IW crests and IW troughs are shown in Figure 30. It is seen from this figure that the intensities of the lowest harmonics for IW crests and IW troughs are close to each other, while the intensities of high-order harmonics are strongly different over IW crests and troughs. To estimate quantitatively the modulation of GCW, the GCW spectra were processed as follows. The spectral intensity of different harmonics in the current GCW spectrum was calculated in a given frequency band around a central n-th harmonic frequency taking into account the Doppler shift of the n-th harmonic due to IW orbital currents. Figure 31 presents an IW record, the frequency of the first spectral peak in the current GCW spectrum corresponding to the basic harmonic, and the spectral intensity of the basic and the 17th harmonics of GCW.

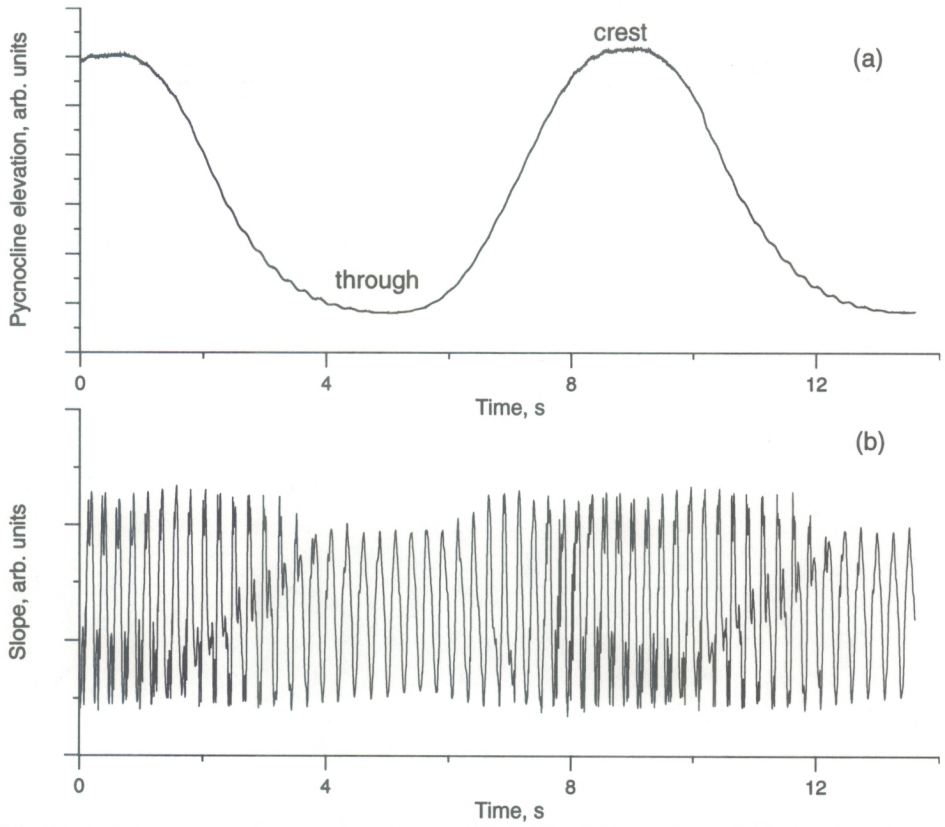

Fig. 29. Simultaneous records of pycnocline elevations due to IW (a) and surface wave slopes (b). (SW generator amplitude - 1.8 mm, IW amplitude – 1 cm)

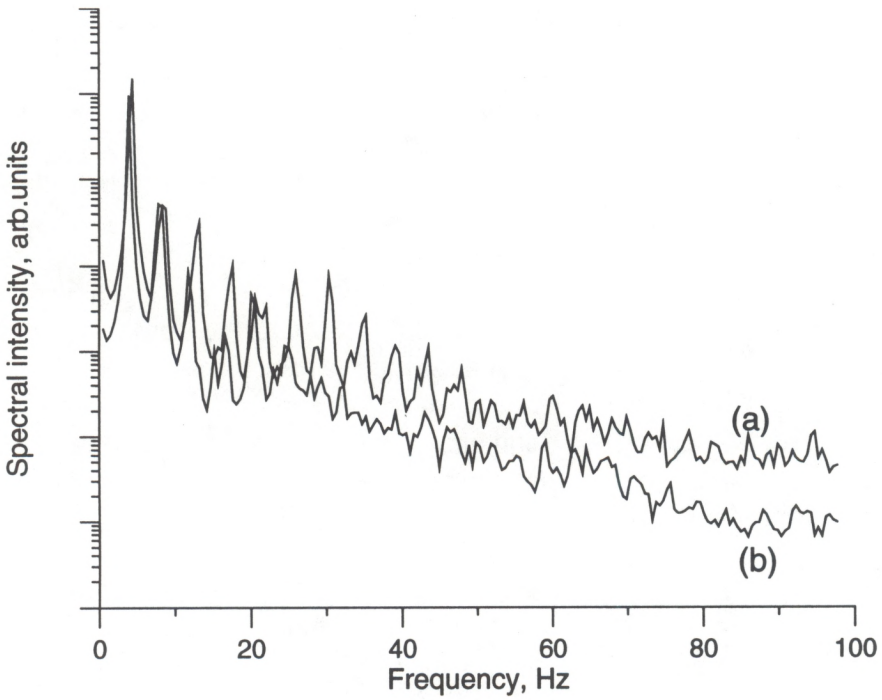

Fig. 30. Spectrum of GGW (see Fig.29) over IW troughs (b) and IW crests (a) .

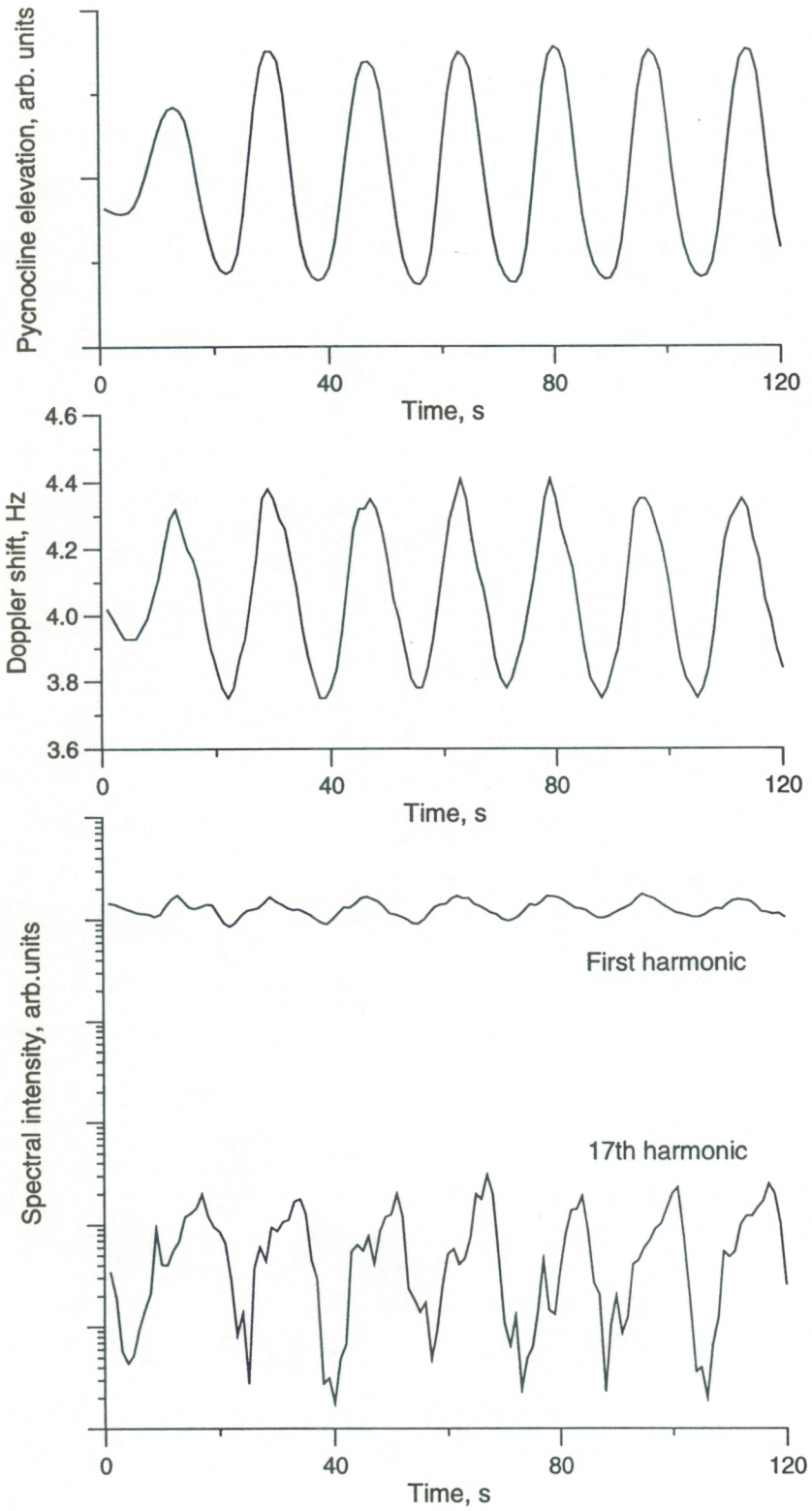

Fig. 31. IW record, the frequency of the basic harmonic in the current GCW spectrum, and the spectral intensity of the basic and the 17th harmonics of GCW.

The modulation coefficient M_n of the n-th harmonic can be defined as

$$M_n = (a_n^{max} - a_n^{min}) / (a_n^{max} + a_n^{min}).$$

Here a_n^{max}, a_n^{min} denote maximum and minimum spectral amplitudes (the square root of the spectral intensity) of the n-th harmonic of GCW. The modulation coefficient of the basic and 17th harmonics obtained in both sets of the experiments as a function of the basic GCW amplitude is shown in Figure 32.

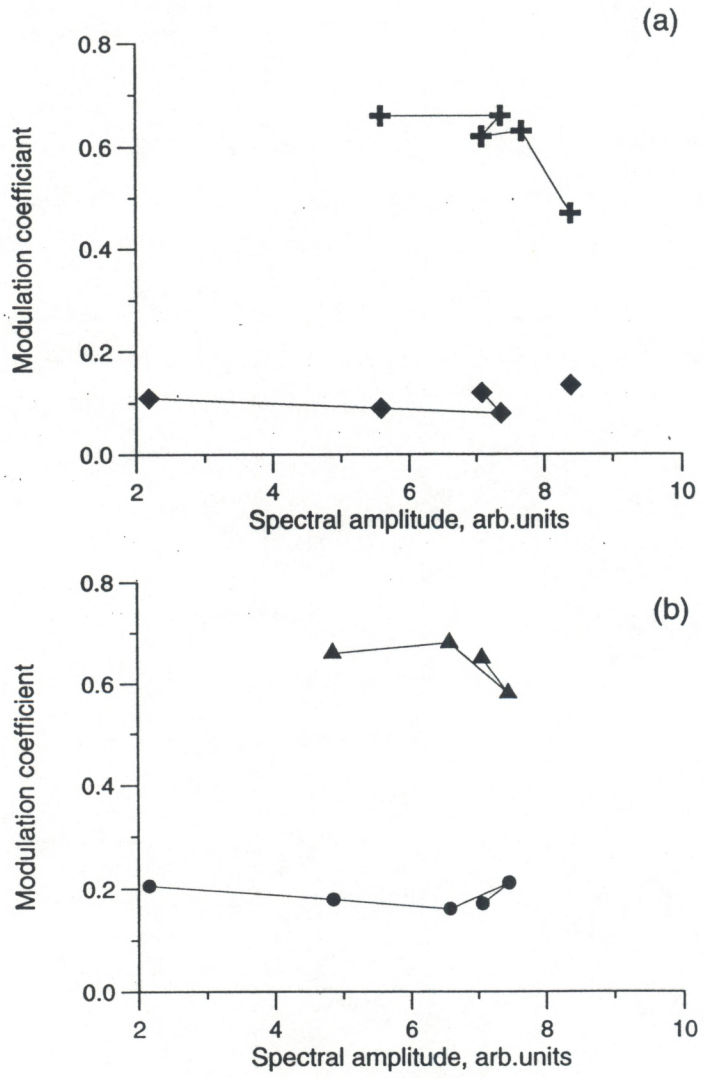

Fig. 32. Modulation coefficient of the basic and the 17th harmonic of GCW as a function of the basic GCW amplitude for two different IW amplitudes
(a - 2 mm, b - 4 mm, ●,◆ - first harmonic, ✚,▲ - 17th harmonic)

As expected, the modulation coefficient of the "parasitic" ripples essentially (up to 5-7 times) exceeds the modulation coefficient of the basic GCW. Note that the difference in the modulation coefficients for spectral intensities is even higher. It follows from Figure 32 that modulation of the basic GCW increases with the amplitude of IW, while for the "parasitic" ripples the modulation coefficient values are practically equal for the two IW amplitudes. For linear GCW the modulation coefficient due to the kinematic modulation mechanism is proportional to the amplitude of IW (see, Lewis et al., 1974, Ermakov and Salashin, 1984). For the "cascade" mechanism the modulation coefficient of high order harmonics is much larger than the "kinematic" modulation coefficient of basic GCW and, as one can expect from the dependence of the harmonic amplitudes on the basic GCW amplitude (see Fig. 28) the cascade modulation coefficient has practically no dependence on the IW amplitude. The normalized modulation coefficient, M/β (β is the non-dimensional IW amplitude which is equal to U/C, where U denotes the IW orbital velocity amplitude and C the IW phase velocity) is plotted in Figure 33 and shows that M/β does not depend on IW amplitude for the basic GCW harmonic and decreases with IW amplitude for high- order harmonics.

The described peculiarities of the "cascade" modulation, presented above for the 17th harmonic (frequency of order of 70 Hz, which is typical for the frequencies of "parasitic" capillary ripples) are similar for other high-order harmonics. Figure 34 presents the modulation coefficient as a function of a harmonic number. M-values grow fast with n for small n and practically do not depend on frequency for harmonics with $n >$ (8-10).

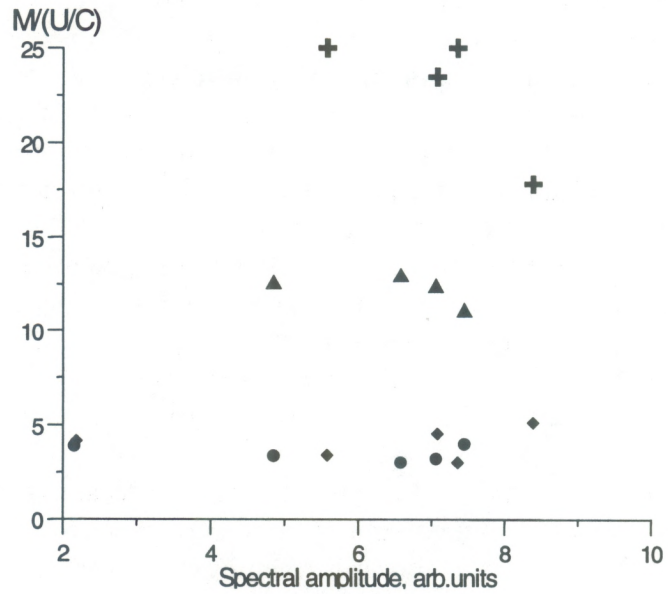

Fig. 33. The normalized modulation coefficient.
(2mm IW ampl.: ◆ - first harmonic, ✚ - 17 th harmonic,
4 mm IW ampl.: ● - first harmonic, ▲ - 17 th harmonic).

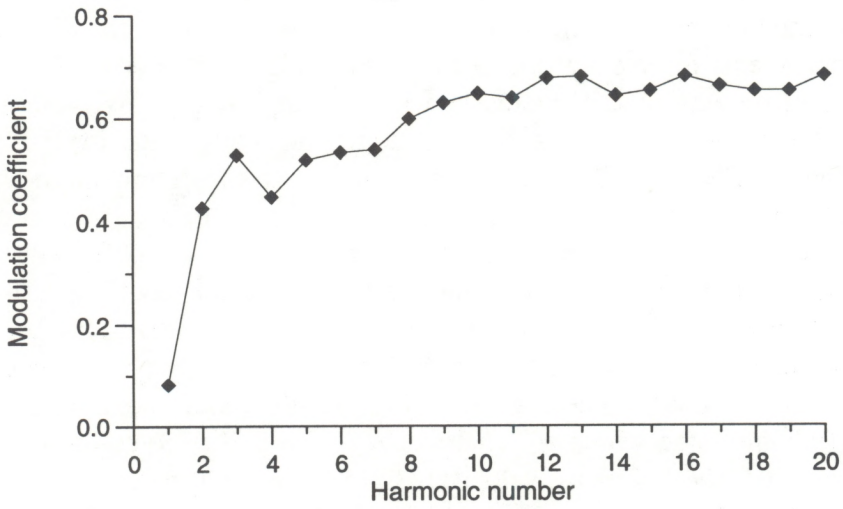

Fig. 34. Modulation coefficient as a function of a harmonic number (IW amplitude -1mm).

5. Conclusions.

Modulation of periodic mechanically generated gravity-capillary waves (GCW) under the action of internal waves has been studied in an oval wave tank of IAP. A new mechanism of strong ("cascade") modulation of short (mm-cm-scale) waves has been modelled. It has been shown that the modulation coefficient of high-order harmonics of GCW under the action of internal waves significantly exceeds the modulation coefficient of the basic GCW. This strong "cascade" modulation is explained by a sharp dependence of the amplitudes of high-order harmonics on the amplitude of the basic GCW.

The proposed modulation mechanism can explain strong modulation of short cm-scale waves due to internal waves observed in field experiments, in particular, in radar measurements of surface manifestations of internal waves. Note that the suggested mechanism of strong modulation of short GCW was investigated in our wave-tank experiments only for the simplest case of modulation of quasi-monochromatic surface waves.

Modulation of wind waves is expected to be more complex, because the spectrum of short (cm-mm-scale) wind waves is formed both by free surface waves (obeying the linear dispersion relation of GCW) and by nonlinear harmonics of longer dm-scale GCW (see Ermakov et al., 1998). Therefore, the resulting modulation of short centimeter-scale wind waves due to IW is expected to be determined by hydrodynamic modulation of free wind waves and by the "cascade" modulation of bound wave components. Investigation of modulation of steep wind waves can be a subject of further studies.

References

Basovich, A.Ya., V.V. Bakhanov, and V.I. Talanov, 1982. Effect of intense internal waves on wind waves (a kinematic model). In *"The Action of Intensive Internal Waves on the Sea Surface"*, Gorky, IPF AN SSSR, no. 8. [In Russian].

Bogatyrev, S.D., V.V. Bakhanov, I.S. Dolina, S.A. Ermakov, E.A. Gromov, L.A. Ostrovsky, V.V. Papko, V.I. Talanov, Y.I. Troitskaya, V.V. Titov, and D.V.Zaborskikh, 1997. Laboratory modeling and theoretical studies of wave processes in the ocean. Part1: Experimental Design and Program (L.A. Ostrovsky, Editor). *NOAA Technical Memorandum ERL ETL-278,* Environmental Technology Laboratory, Boulder, Colorado.

Briggs, R.J., 1964. Electron stream interaction with plasma. *Research Monograph No. 29*, MIT Press., Cambridge, Mass.

Engevik, L., 1982. An amplitude-evolution equation for linearly unstable modes in stratified shear flows. *J. Fluid Mech*, **117:** 457-471.

Ermakov, S.A., E.N.Pelinovsky and T.G. Talipova, 1982. Film Mechanism of the Internal Wave Action on Wind Ripples, *in "The Action of Intensive Internal Waves on the Sea Surface"*, Gorky, IPF AN SSSR, 31. [In Russian].

Ermakov, S.A. and. S.G. Salashin, 1984. Modulation of Gravity-Capillary Waves in the Internal Wave Field, Izv. AN SSSR, *Fiz. Atm. Okeana*, **20:** 394 [In Russian].

Ermakov, S.A.,. K.D.Ruvinsky, S.G.Salashin, G.I. Freidman, 1986. Experimental Study of Capillary-Gravity Wave Generation by Steep waves on Deep Water, *Izv. AN SSSR, Fiz. Atm. Okeana*, **22:** 1072 [In Russian].

Ermakov,S.A., I.A.Sergievskaya, E.M.Zuikova, V.Yu.Goldblat, Yu.B.Shegol'kov and J.C.Scott, 1998. Wave Tank Optical Measurements of Phase Velocities of Wind Waves In *Sensing and Managing the Environment, IEEE Intern. Geoscience and Remote Sensing Symp. Proc.*, Seattle, Washington, v.5.

Gossard, E.E. and H. Hooke, 1975. Waves in the atmosphere. Elsevier Scientific Publishing Company.

Huerre, P.,and P.A. Monkewitz, 1985. Absolute and convective instabilities in free shear layers. *J. Fluid Mech,* **159:** 151-168.

Huerre, P.,and P.A. Monkewitz, 1990. Local and global instabilities in spatially developing flows. *Ann. Rev. Fluid Mech.*, **22:** 473-537.

Koop, G.C., and F.K. Browand, 1979. Instability and turbulence in a stratified fluid with shear. *J. Fluid Mech.*, **93(1),** 135-159.

Lewis, J.E., B.M. Lake and D.R.S. Ko, 1974. On the interaction of internal waves and surface gravity waves. *J. Fluid Mech*, **63(4):** 773-800.

Leib, S.I, Goldstein, M.E. , 1986. The generation of capillary instabilities on a liquid jet. *J. Fluid Mech.*, **159:** 151-168.

Moiseev, S.S., V.G. Pyngin, R.Z. Sagdeev, N.V.Suyazov, A.V. Tur, and V.V. Yanovsky, 1983. Secondary and correlation instabilities in continuous systems. In *Nonlinear Waves. Self-Organization* , Moscow, Nauka, 264 p.

Moiseev, S.S., V.G. Pyngin, N.V Suyazov, and V.S. Etkin, 1984. "Explosive" interaction of the zero-energy waves. *Izvestiya AN SSSR, Atmospheric and Oceanic Physics*, **20(9)**: 842-847.

Moiseev, S.S., V. G. Pyngin, and N. V. Suyazov, 1986. The features of nonlinear wave interactions n the Kelvin-Helmholtz flow when the parameters tend to the boundary of stability. *Preprint of ISR RAS,* No.1176, 15 p.

Monkewitz, P.A., 1990. The role of absolute and convective instability in predicting the behavior of fliud systems. *Eur. J. Mech., B/Fluids.* **9(5):** 395-413.

Monkewitz, P.A., and L.N. Nguyen, 1987. Absolute instability in the near wake of two-dimensional bluff bodies. *J. Fluid Struct.*, **1:** 165-184.

Monkewitz, P.A., and K.D. Sohn, 1986. Absolute instability in hot jets and treir control. *AIAA*, No. 86, 1882.

Ostrovsky, L. A., S. A. Rybak, and L. Sh. Tsimring, 1986. Negative energy waves in hydrodynamics. *Sov. Phys. Uspekhi*, **29(11):** 1040-1052.

Perlin, M., H. Lin, and C-L. Ting, 1993. On parasitic capillary waves generated by steep gravity waves: an experimental investigation with spatial and temporal measurements. *J. Fluid Mech.*, **2:** 417-445.

Showalter, D.C., C.W. Van-Atta, and J.C. Lasheras, 1994. A study of streamwise vortex structure in a stratified shear layer. *J. Fluid Mech.*, **281:** 247-291.

Voronovich, A.G., and S.A Rybak, 1978. Explosive instability of the stratified shear flow. *Dokl. AN SSSR*, **239(6):** 1457-1460.

Voronovich, A.G., E.V. Lobanov, and S.A. Rybak, 1980. On stability of gravity-capillary waves in the presence of vertically inhomogeneous flow. *Izvestiya AN SSSR, Atmospheric and Oceanic Physics*, **16(3):** 330-331.

*U.S. GPO 2000-0-673-019/40181